The Meteoritical Society

Meteoritics & Planetary Science 1–38 (2014)
doi: 10.1111/maps.12323

Fall, recovery, and characterization of the Novato L6 chondrite breccia

Peter JENNISKENS[1,2*], Alan E. RUBIN[3], Qing-Zhu YIN[4], Derek W. G. SEARS[2,5], Scott A. SANDFORD[2], Michael E. ZOLENSKY[6], Alexander N. KROT[7], Leigh BLAIR[1], Darci KANE[8], Jason UTAS[9], Robert VERISH[10], Jon M. FRIEDRICH[11,12], Josh WIMPENNY[4], Gary R. EPPICH[13], Karen ZIEGLER[14], Kenneth L. VEROSUB[4], Douglas J. ROWLAND[15], Jim ALBERS[1], Peter S. GURAL[1], Bryant GRIGSBY[1], Marc D. FRIES[6], Robert MATSON[16], Malcolm JOHNSTON[17], Elizabeth SILBER[18], Peter BROWN[18], Akane YAMAKAWA[4], Matthew E. SANBORN[4], Matthias LAUBENSTEIN[19], Kees C. WELTEN[20], Kunihiko NISHIIZUMI[20], Matthias M. M. MEIER[21,22], Henner BUSEMANN[23], Patricia CLAY[23], Marc W. CAFFEE[24], Phillipe SCHMITT-KOPPLIN[25,26], Norbert HERTKORN[25], Daniel P. GLAVIN[27], Michael P. CALLAHAN[27], Jason P. DWORKIN[27], Qinghao WU[28], Richard N. ZARE[28], Monica GRADY[29], Sasha VERCHOVSKY[29], Vacheslav EMEL'YANENKO[30], Sergey NAROENKOV[30], David L. CLARK[18], Beverly GIRTEN[2], Peter S. WORDEN[2]
(The Novato Meteorite Consortium)

[1]SETI Institute, Carl Sagan Center, Mountain View, California 94043, USA
[2]NASA Ames Research Center, Moffett Field, California 94035, USA
[3]Institute of Geophysics and Planetary Physics, UCLA, Los Angeles, California 90095–1567, USA
[4]Department of Earth and Planetary Sciences, University of California at Davis, Davis, California 95616–8605, USA
[5]BAER Institute, Mountain View, California 94043, USA
[6]Astromaterials Research and Exploration Science, NASA Johnson Space Center, Houston, Texas 77801, USA
[7]Hawai'i Institute of Geophysics and Planetology, University of Hawai'i at Manoa, Honolulu, Hawai'i 96822, USA
[8]Buck Institute, Novato, California 94945, USA
[9]Institute of Geophysics and Planetary Physics, UCLA, Los Angeles, California 90095–1567, USA
[10]Meteorite Recovery Laboratory, P.O. Box 463084, Escondido, California 92046, USA
[11]Department of Chemistry, Fordham University, Bronx, New York 10458, USA
[12]Department of Earth and Planetary Sciences, American Museum of Natural History, New York, New York 10024, USA
[13]Lawrence Livermore National Laboratory, Glenn Seaborg Institute, Livermore, California 94550, USA
[14]Institute of Meteoritics, University of New Mexico, Albuquerque, New Mexico 87131–0001, USA
[15]Center for Molecular and Genomic Imaging, University of California at Davis, Davis, California 95616, USA
[16]S.A.I.C., San Diego, California 92121, USA
[17]US Geological Survey, Menlo Park, California 94025, USA
[18]Department of Physics & Astronomy, University of Western Ontario, London, Ontario N6A 3K7, Canada
[19]Lab. Naz. del Gran Sasso, Inst. Naz. di Fiscia Nucleare, I-67010 Assergi (AQ), Italy
[20]Space Sciences Laboratory, University of California, Berkeley, California 94720, USA
[21]Department of Earth Sciences, ETH Zürich, CH-8092 Zürich, Switzerland
[22]Department of Geology, Lund University, SE-22362 Lund, Sweden
[23]School of Earth, Atmospheric and Environmental Sciences (SEAES), University of Manchester, Manchester M13 9PL, UK
[24]Department of Physics, Purdue University, West Lafayette, Indiana 47907, USA
[25]B.G.C., Helmholtz Zentrum München, D-85764 München, Germany
[26]A.L.C., Technische Universität München-TUM, D-85354 Freising, Germany
[27]Solar System Exploration Division, NASA Goddard Space Flight Center, Greenbelt, Maryland 20771, USA
[28]Department of Chemistry, Stanford University, Stanford, California 94305–5080, USA
[29]Planetary and Space Science Research Institute, Open University, Milton Keynes MK7 6AA, UK
[30]Institute of Astronomy of the Russian Academy of Sciences (INASAN), Moscow 119017, Russia
[*]Corresponding author. E-mail: petrus.m.jenniskens@nasa.gov

(Received 30 December 2013; revision accepted 07 May 2014)

Abstract–The Novato L6 chondrite fragmental breccia fell in California on 17 October 2012, and was recovered after the Cameras for Allsky Meteor Surveillance (CAMS) project determined the meteor's trajectory between 95 and 46 km altitude. The final fragmentation from 42 to 22 km altitude was exceptionally well documented by digital photographs. The first sample was recovered before rain hit the area. First results from a consortium study of the meteorite's characterization, cosmogenic and radiogenic nuclides, origin, and conditions of the fall are presented. Some meteorites did not retain fusion crust and show evidence of spallation. Before entry, the meteoroid was 35 ± 5 cm in diameter (mass 80 ± 35 kg) with a cosmic-ray exposure age of 9 ± 1 Ma, if it had a one-stage exposure history. A two-stage exposure history is more likely, with lower shielding in the last few Ma. Thermoluminescence data suggest a collision event within the last ~0.1 Ma. Novato probably belonged to the class of shocked L chondrites that have a common shock age of 470 Ma, based on the U,Th-He age of 420 ± 220 Ma. The measured orbits of Novato, Jesenice, and Innisfree are consistent with a proposed origin of these shocked L chondrites in the Gefion asteroid family, perhaps directly via the 5:2 mean-motion resonance with Jupiter. Novato experienced a stronger compaction than did other L6 chondrites of shock-stage S4. Despite this, a freshly broken surface shows a wide range of organic compounds.

INTRODUCTION

On the evening of Wednesday October 17, 2012, a bright fireball was widely observed and photographed from locations in and around the San Francisco Bay Area. Following the fireball sighting, six meteorites were recovered in the town of Novato (Fig. 1). The meteorite is an L6 ordinary chondrite fragmental breccia of shock-stage S4, composed of dark and light lithologies (Fig. 2).

Initial reports in the media put the impact location erroneously in the hills north of Martinez, CA. Fortunately, the fireball crossed the camera fields of NASA's CAMS program. This video surveillance of the night sky measures meteoroid trajectories over California to map the meteor showers throughout the year (Jenniskens et al. 2011). The calculated downward projected path predicted that 1 g fragments fell near Bolinas, 100 g fragments near Novato, and 1 kg fragments near Sonoma.

The CAMS-derived trajectory was published in the *San Francisco Chronicle*, initially online on Friday evening, 19 October (see Fig. 11 below). Novato resident Lisa Webber read the article and remembered hearing the sound of an object hitting the roof of her garage multiple times ("tok-tok-tok-tok") that previous Wednesday night. At the time, she entered the garage thinking raccoons were knocking over objects, but no such disturbance was found. After reading the newspaper article, she searched her yard for possible meteorites on Saturday October 20. She examined the roof and while climbing down the ladder, she noticed a dense 61.9 g stone near the foot of the ladder (now called Novato N01), which reacted strongly to a permanent magnet.

This Novato meteorite was difficult to distinguish from weathered terrestrial rocks, because the dark lithology did not retain its fusion crust (Fig. 1). Searching for corroborating evidence of an impact at the Webber residence that evening, Webber's neighbor Luis Rivera identified an impact divot. That divot had a shape and location consistent with a meteorite from this fall first hitting the roof above the study room on one side of the U-shaped house, then being deflected to the roof over the garage on the other side, where it bounced into the air several times before landing next to the garage. Indeed, a second smaller divot was found later, on the side of the garage roof opposite to the study.

A second 65.8 g stone was found in Novato (N02) by Brien Cook on Monday October 22. It was initially discarded, but subsequent to reports of the Webber find, it was retrieved, cut, and recognized as a meteorite on October 24. Four more individual meteorites were recovered on pavement in the following weeks (Fig. 1). An overview of these finds is given in Table 1.

An airship search was commenced along a line from Novato to the geometric impact point, and then back to Sonoma. Deployed from NASA Ames Research Center, the airship Eureka travelled at a 300 m altitude. Two spotters searched the terrain for impact scars from falling 1–10 kg meteorites over a region ±1 km from the path. After consultation with the local landowners, some potential sites were investigated, but no confirmed impacts were located.

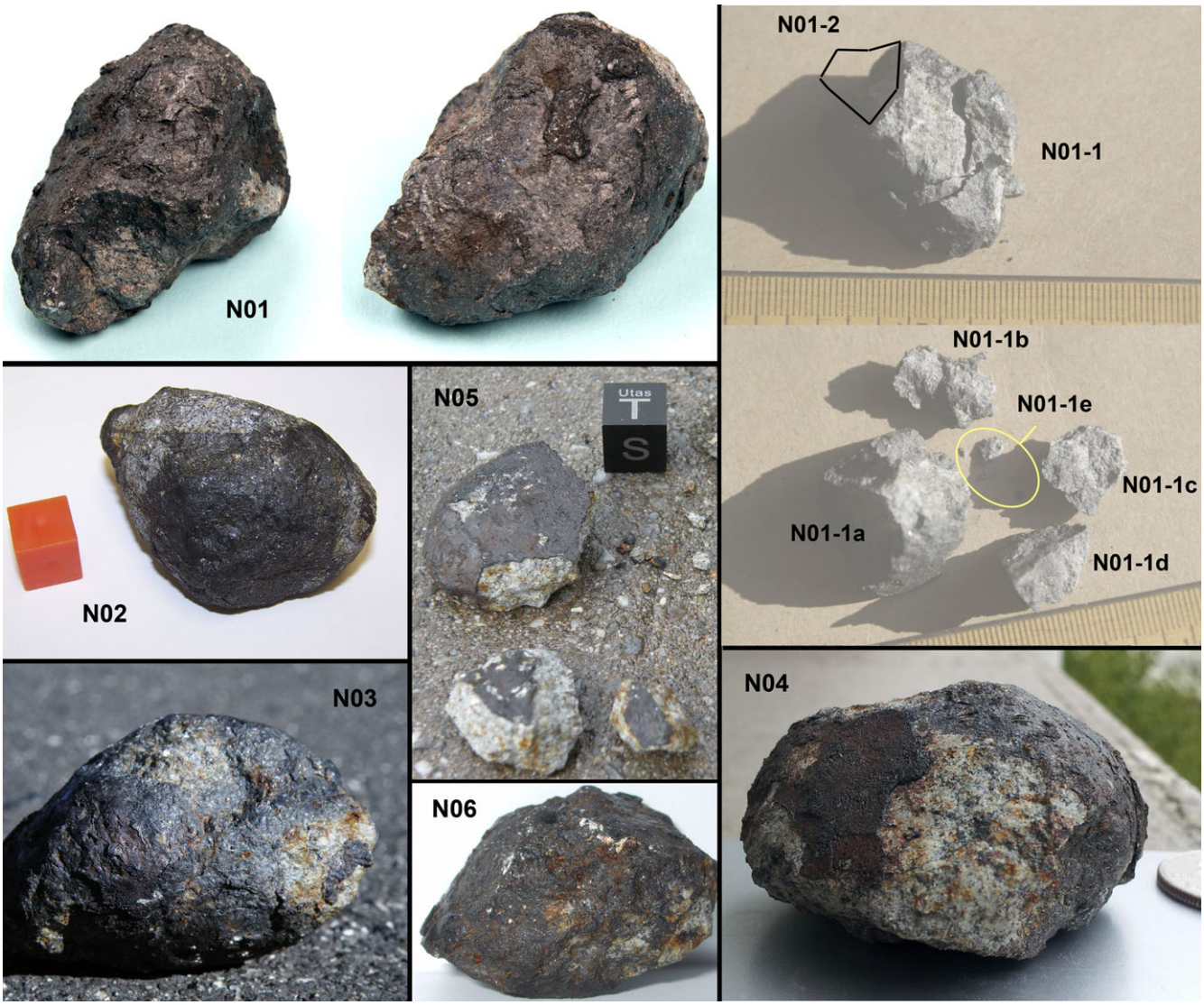

Fig. 1. All recovered Novato meteorites, with sample identification chart for Novato N01 (scale in mm). N01 is shown in two different orientations. Note the fusion crust and manifestation of light and dark lithologies in the individual meteorites. Scale cubes are 1 cm in diameter, while the coin in the panel of N04 is a U.S. quarter. Scales for N06 and N03 are shown in Figs. 2 and 16.

This exceptionally well-observed fall and fresh meteorite recovery led us to assemble a Novato Meteorite Consortium to further the recovery of the meteorites and do the preliminary analysis reported here (http://asima.seti.org/n/). This analysis is focused on characterization and aspects that might forge a link between L-group chondrites and the asteroid family of their parent body.

MATERIALS AND METHODS

Parts of Novato N01 (type specimen) and N06 were made available for destructive analysis, while samples N02–N05 were available for nondestructive analysis. Sample N01 was broken in a controlled break using a Southwark-Emery Tensile Machine at NASA Ames Research Center. The fragment identifications are listed in Fig. 1. The fragment notation "N01-1e" refers to the 5th sample taken from fragment #1 obtained when meteorite N01 was broken. Fragment N01-1a is the type specimen, now stored at the University of California, Los Angeles (UCLA). Meteorite N06 was cut at the University of California, Davis (UC Davis) to create slices. On request, fragments and slices were distributed to the consortium members, and among consortium

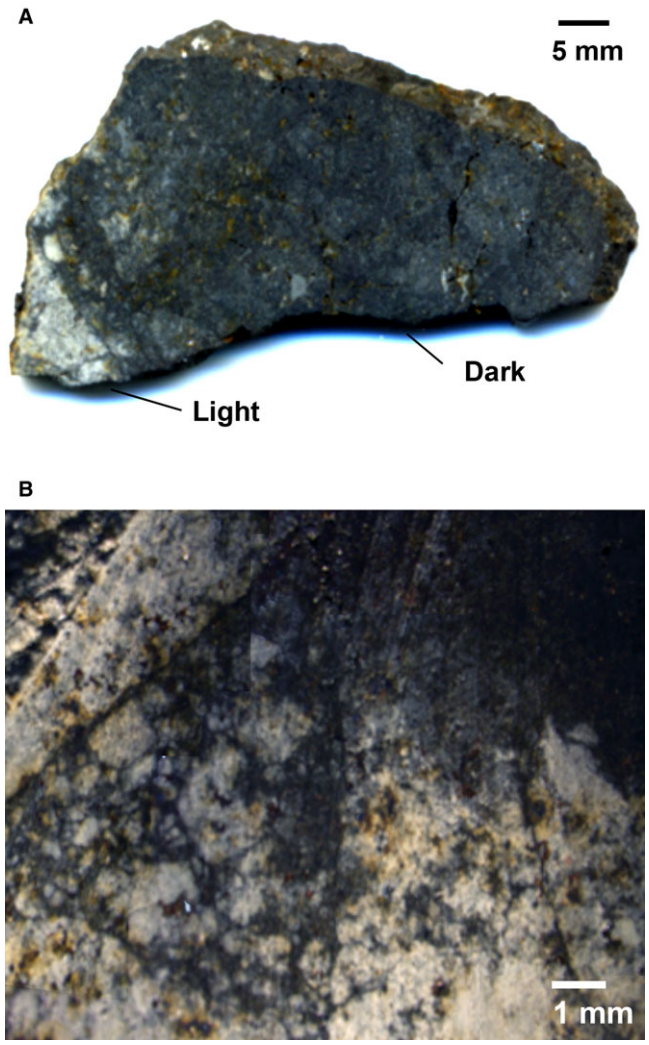

Fig. 2. Photographic images of cut Novato faces showing the brecciated chondritic texture with light and dark lithologies distributed unevenly. Boundaries between them can be sharp or gradual. A) Contrast-enhanced image of a slice of Novato N06. B) Same for Novato N02, with cut marks at center top and in top left corner.

members, coordinating the distribution so that the same samples were analyzed using complementary techniques.

METEORITE PROPERTIES AND CLASSIFICATION

Mechanical Properties and Magnetic Susceptibility

Of key interest are the mechanical and physical properties that play a role in the fragmentation during entry (Consolmagno et al. 2008). During the controlled break, the quasi-static compressive strength of Novato N01 was measured at 1100 ± 250 MPa. This value is much higher than the typical 100–200 MPa measured for ordinary chondrites (Slyuta 2010). The uncertainty reflects the irregular loading of the surface area that was evident from the meteorite imprint on aluminum foil between sample and pressure surface.

At the Buck Institute, the density of N06 was measured in water at 3.4 ± 0.2 g cm^{-3}. Volumes of samples N06 (mostly dark lithologies) and N05 (light) were measured by high-resolution X-ray computed tomography at the Center for Molecular and Genomic Imaging at UC Davis (Fig. 3). Total volumes were calculated to be 4.46 and 7.12 cm^3 for N05 and N06, respectively. The samples did not have significant fusion crust. The corresponding densities are 3.21 ± 0.02 and 3.32 ± 0.02 g cm^{-3}, which are in good agreement with the average bulk density of 3.35 ± 0.16 g cm^{-3} for ordinary L chondrites (Britt and Consolmagno 2003; Consolmagno et al. 2008). Porosity in L chondrites is primarily in the form of microcracks, whose sizes are below the 15–40 μm resolution of the CT volumes collected here. Most other shocked L chondrites have microporosities in the 3–5% range (Britt and Consolmagno 2003; Consolmagno et al. 2008; Friedrich and Rivers 2013).

Magnetic susceptibility (χ) was measured on six samples at UC Davis (Table 1). To some extent, the measured values of individual samples varied with their orientation in the susceptibility bridge, suggesting that the susceptibility is somewhat anisotropic, a phenomenon reported before for other ordinary chondrites (e.g., Morden and Collinson 1992), when deformation and other processes cause anisotropic

Table 1. Overview of recovered meteorites.

#	Mass (g)	$<\log \chi > (10^{-9}$ kg $m^3)$	Latitude (°N)	Longitude (°W)	Condition of find	Date	Finder
N01	61.9	4.20 ± 0.02	38.1090	122.6105	Individual	10/20/2012	Lisa Webber
N02	65.9	4.16 ± 0.02	38.0941	122.5683	Individual	10/22/2012	Brien Cook
N03	79.8	–	38.1152	122.5640	Individual + <1 g fragment	10/27/2012	Jason Utas
N04	107	–	38.1217	122.5670	Individual	10/27/2012	Robert Verish
N05	24.3	4.32 ± 0.04	38.1195	122.5720	Found broken in 3+ fragment	11/02/2012	Jason Utas
N06	23.7	4.34 ± 0.03	38.0768	122.5692	Individual	11/11/2012	Darci Kane

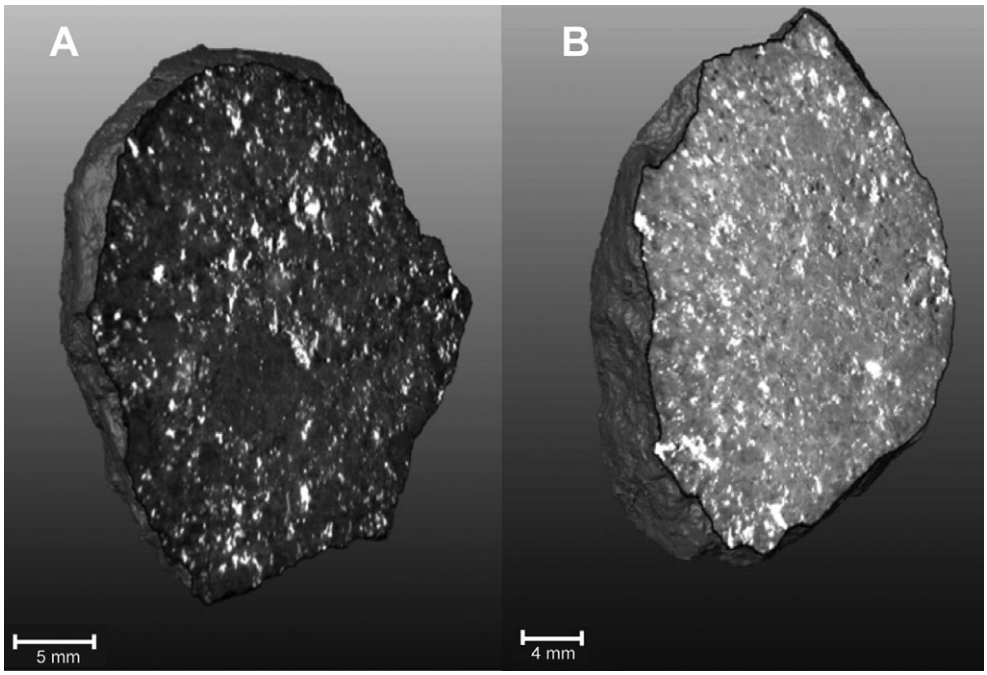

Fig. 3. X-ray CT imagery of Novato N05 and N06, with light patches showing X-ray opaque metal grains (FeNi) or sulfides (troilite, FeS). A) A computer sliced X-ray view of the interior of N05 of pure light lithology, one of 1824 X-ray CT slices in this viewing direction with a pixel size of 15.28 μm. B) A computer sliced X-ray view of the interior of N06 of mostly dark lithology, one of 1003 X-ray CT slices in this viewing direction with a pixel size of 44.12 μm. See supporting information for online 3-D movie rendition of the two stones, full experimental details, and movie captions. Additional information can be obtained at http://www.youtube.com/user/YinLabatUCDavis.

mineral and magnetic domain structure. Depending on orientation of the samples, values of log χ ranged from 4.08 to 4.46 (where χ is measured in units of 10^{-9} m^3 kg^{-1}), with mean values for the different stones ranging from $\chi = 4.16$ to 4.34. This range is below the range (4.75–4.95) for L6 meteorites as reported by Rochette et al. (2003). Based on the magnetic susceptibility, Novato would be classified as a typical LL chondrite. Other evidence will now be presented that classifies Novato as an L chondrite, instead.

Petrography and Mineralogy

Details of the brecciated texture of Novato, with unevenly distributed light and dark lithologies, are shown in Fig. 2. A slice of Novato N02 examined at UCLA contained approximately 55 vol% chondritic clasts and approximately 45 vol% shock-darkened material. Some parts show light angular clasts in a dark matrix. A slice from Novato N06 showed mainly dark lithology, itself composed of many clasts (Fig. 2). Figures 4A–F show backscattered electron (BSE) images and combined X-ray elemental maps of this slab, taken at the University of Hawai'i at Manoa.

The fragment initially examined for petrography at UCLA was from Novato N01. Silicates exhibit weak mosaic extinction, characteristic of a moderate shock-stage S4, corresponding to an equilibrium shock pressure of ≥10–15 GPa (Stöffler et al. 1991). No maskelynite was seen that would be indicative of S5, and there is little or no silicate melting indicative of shock-stage S6. Plagioclase grains range from 50 to 200 μm, consistent with petrologic type 6 (Van Schmus and Wood 1967).

The dark areas are highly shocked, but not melted; relict chondrules are still visible. The dark color (silicate darkening) is due to extensive crosscutting of silicate grains by troilite veins (e.g., Rubin 1992; Simon et al. 2004). Most chromite grains are fractured; like the silicates, many chromite grains are transected by troilite veins as is common in S3–S6 chondrites (Rubin 2003). Also common in such chondrites are chromite-plagioclase assemblages (Rubin 2003), a few of which occur in Novato (Figs. 4D and 4E). One 12 × 20 μm-size grain of metallic Cu was found. Some of the troilite grains are polycrystalline, consistent with shock-stage S4–S5 (Schmitt et al. 1993; Bennett and McSween 1996). There are regions of localized plagioclase melting, especially around metal and sulfide grains. A few silicate shock melt veins are present that contain small metal and sulfide blebs, consistent with shock-stage S4–S6 (Stöffler et al. 1991).

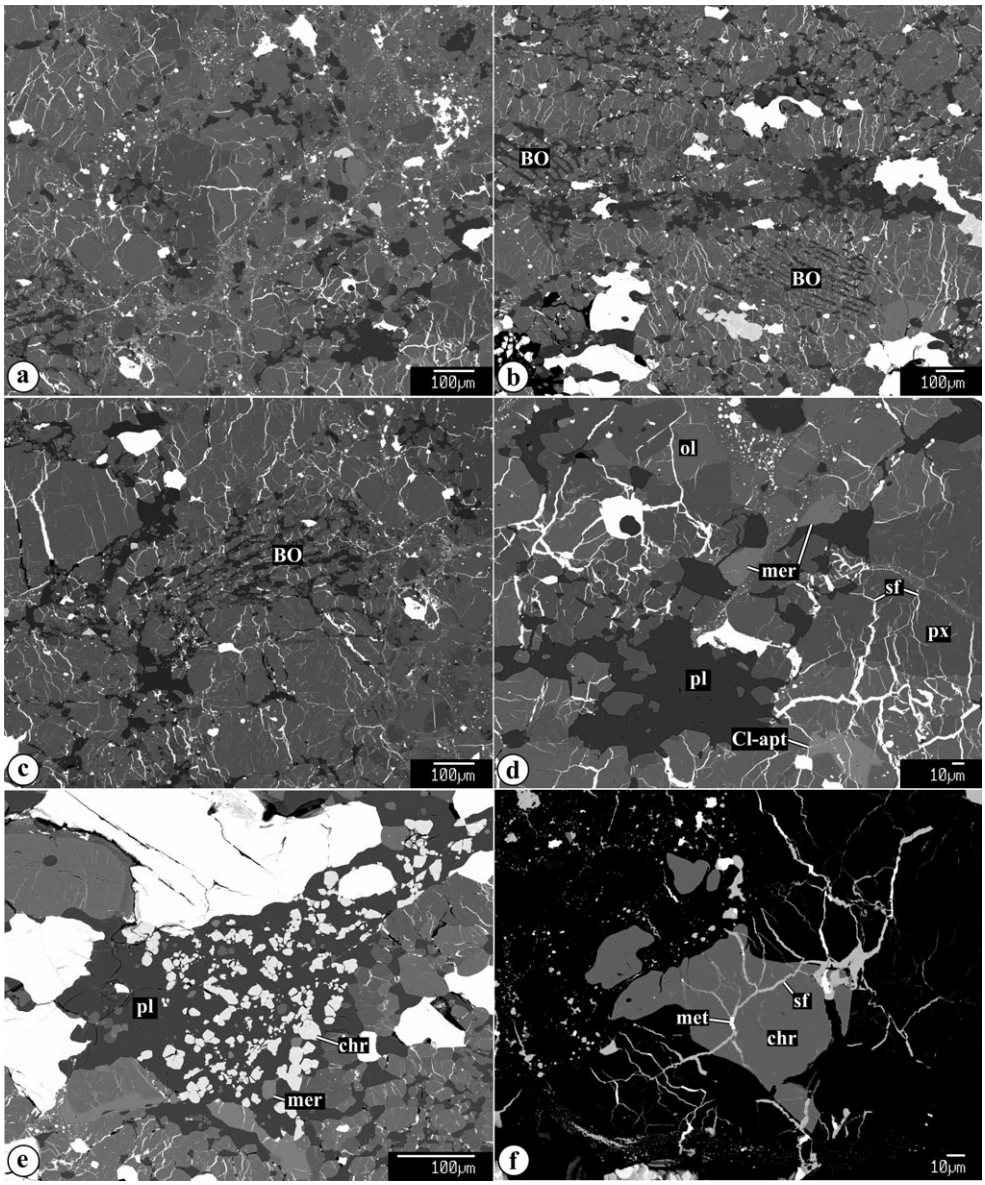

Fig. 4. Backscattering electron (BSE) images of Novato N06. A) The meteorite is extensively recrystallized due to thermal metamorphism and contains abundant coarse grains of plagioclase, phosphates, and chromite; B–C) Only rare barred olivine chondrules can be recognized in BSE images; D–E) The presence of plagioclase-chromite-phosphate pockets are also visible; F) Abundant sulfide/metal veins crosscutting silicate and chromite grains suggest that the meteorite experienced extensive shock metamorphism after thermal metamorphism. chr = chromite; Cl-apt = Cl-apatite; met = Fe,Ni-metal; ol = olivine; pl = plagioclase; px = low-Ca pyroxene; sf = troilite; mer = merrillite.

The lighter colored areas are also appreciably shocked, but have far fewer troilite veins transecting them. These light-colored chondritic clasts contain moderately large, highly recrystallized barred olivine (BO) (Figs. 4B and 4C) and porphyritic olivine-pyroxene (POP) chondrules that are well integrated into the matrix, consistent with petrologic type 6. These chondritic clasts are much lighter colored in transmitted light than the matrix of the rock.

The mineral compositions of olivine ($Fa_{24.1 \pm 0.4}$, $n = 21$) and low-Ca pyroxene ($Fs_{20.7 \pm 0.5}$ $Wo_{1.5 \pm 0.2}$, $n = 22$) are characteristic of L-group chondrites (Rubin 1990; Brearley and Jones 1998). Also present among the mafic silicates is high-Ca pyroxene ($Fs_{8.0 \pm 0.7}$ $Wo_{44.7 \pm 0.8}$, $n = 5$). Chromite grains ($n = 11$) are somewhat richer in Al_2O_3 (6.4 wt%) and MgO (3.4 wt%) than unshocked ordinary chondrite chromite (Bunch et al. 1967), but are more characteristic of shocked

Table 2. Summary of XRF-derived major elemental composition data for Novato N06 (slab), measured for areas with predominantly dark lithology and light lithology on the front and back of the slab.

	Dark (front)		Dark (back)		Light (front)		Light (back)	
	Mean	1σ (%)	Mean	1σ (%)	Mean	1σ (%)	Mean	1σ (%)
Si	18.66	0.73	18.08	0.74	19.48	0.72	18.18	0.74
Fe	17.16	0.24	17.97	0.24	15.67	0.25	17.20	0.24
Mg	16.41	0.66	15.27	0.69	16.33	0.66	15.13	0.69
Al	1.70	2.66	1.77	2.60	2.05	2.39	1.92	2.48
Ca	1.33	1.74	1.24	1.81	1.46	1.67	1.50	1.65
S	1.25	1.99	1.76	1.67	1.67	1.73	1.67	1.72
Na	0.99	5.61	1.02	5.64	1.30	4.81	1.16	5.25
Ni	0.57	1.36	0.67	1.28	0.39	1.61	0.57	1.38
Cr	0.37	2.23	0.33	2.35	0.21	3.03	0.33	2.37
Mn	0.26	2.38	0.24	2.49	0.26	2.36	0.26	2.36
P	0.11	9.93	–	–	0.16	7.94	0.26	6.17
K	0.10	7.03	0.10	7.19	0.10	6.95	0.11	6.61
Ti	0.06	7.44	0.07	7.30	0.06	7.84	0.06	7.89

and shock-melted chromite grains (Rubin 2003). Most of the metallic Fe-Ni is taenite with 21.4 ± 5.4 wt% Ni and 0.51 ± 0.18 wt% Co (n = 18). Only one kamacite grain was identified (7.2 wt% Ni and 1.1 wt% Co). The Co content of this single grain is intermediate between the ranges for L (0.70–0.95 wt% Co) and LL (1.42–37.0 wt% Co) chondrites (Rubin 1990), but is closer to L chondrites. Plagioclase, which has a mean composition of $Ab_{86.0 \pm 0.6}$ $Or_{7.0 \pm 0.4}$ (n = 14), is richer in alkalis than typical ordinary chondrite plagioclase (Van Schmus and Ribbe 1968), and probably reflects shock melting (Rubin 1992). Troilite (n = 10) is essentially pure FeS; it contains no detectable Cr, Co, or Ni.

Bulk Chemical Composition

Chemically, the Novato chondrite is a typical L chondrite. A slice of whole-rock sample of Novato N06 (Fig. 2) was analyzed for major element concentration using a Bruker S8 WD-XRF at Lawrence Livermore National Laboratory. These analyses were performed on two flat cut surfaces on both dark and light lithologies. In general, the results (Table 2) suggest that both light and dark portions of the fragment have very similar major element chemistry, with the following caveat: The XRF at Livermore has a minimum sample size of 8 mm round, which is bigger than the light lithology tip of the Novato 06 fragment (Fig. 2). This means that the "light" analyses are a mixture of both light and dark material (a ratio of about 70:30).

The abundances of 45 trace elements in the Novato meteorite were measured at Fordham University, using the acid dissolution and quadrupole inductively coupled plasma mass spectrometer (Q-ICP-MS) analysis methodology described in Friedrich et al. (2003).

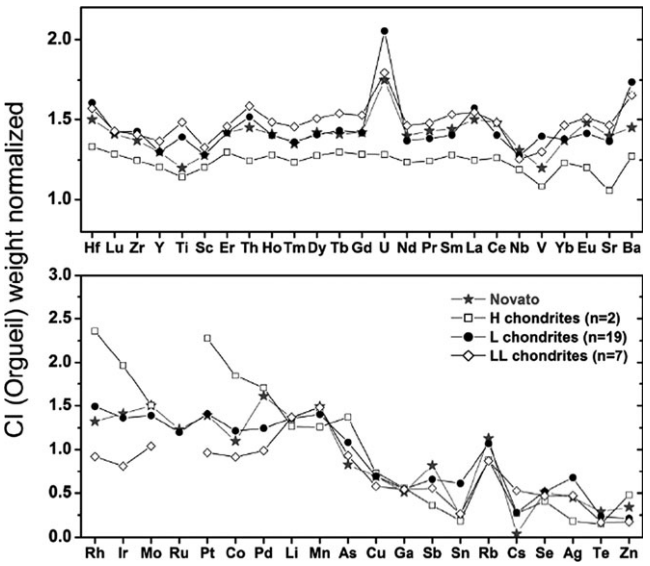

Fig. 5. Mean CI-normalized abundances of lithophiles, siderophiles, and moderately volatile elements in Novato compared with average L chondrite compositions. Elements are organized by increasing putative volatility and similar geochemical character.

Samples analyzed were Novato N01-1e-4 (three aliquots 90.4, 57.6, and 74.7 mg), all dark lithology; N01-2b-6, an aliquot with dark lithology; and a combined aliquot of N01-2b-11, 12, and 17, which consisted of 55% dark and 45% light lithology. The mean lithophile, siderophile, and moderately volatile abundances are presented in Fig. 5 and Table 3. Trace element abundances of averaged values are listed in Table 4. Most important for distinguishing between LL, L, and H chondrites is the mean siderophile abundance. This abundance in Novato is most like that of L chondrites.

Table 3. Preliminary mean CI (Orgueil) weight normalized compositions of lithophiles, siderophiles, and moderately volatile trace elements in Novato, based on using Quadrupole ICP-MS measurements of Novato N01-2b and N01-1e.

Sample	Lithophiles (n = 25)	Siderophiles (n = 6)	Mod. vol (n = 14)
Novato N01-1e-4 (dark)	1.41 ± 0.11	1.37 ± 0.17	0.67 ± 0.44
Novato ~50/50 light/dark N01-2b-11,12,17	1.53 ± 0.38	1.50 ± 1.12	0.64 ± 0.43
H chondrite (n = 2) mean[a]	1.24 ± 0.07	1.94 ± 0.33	0.62 ± 0.44
L chondrite (n = 19) mean[a]	1.45 ± 0.16	1.33 ± 0.11	0.72 ± 0.40
LL chondrite (n = 7) mean[a]	1.48 ± 0.11	0.94 ± 0.08	0.65 ± 0.41

[a]H chondrite mean from Troiano et al. (2011), L (shock-stages S1–S3 only), and LL chondrite mean data from Friedrich et al. (2003, 2004).

The apparent enrichment in uranium is often seen in chondrites, probably because of some sample enriched in phosphate materials, for which U and Th have an affinity.

Using analytical procedures described in Jenniskens et al. (2012) and Popova et al. (2013), we have performed additional wet chemical analyses using the *Element XR* magnetic sector, high-resolution ICP-MS at UC Davis, which offers the possibility to run some elements at higher resolution to avoid potential isobaric interferences. Measured were predominantly light and dark lithology fragments from both N01-1e and N06, and a pure light lithology of Novato N05. Details of the method used and results for Novato and Orgueil are listed in Table 4, and compared with the averaged Q-ICP-MS data obtained at Fordham University.

The rare earth element (REE) patterns of Novato samples normalized to CI chondrites are presented in Fig. 6. The pure light lithologies from N05 and N06 have positive Eu anomalies, with a lower overall REE pattern of 0.8–0.9 compared to CI chondrites (Lodders 2003), whereas the pure dark lithologies from N01 and N06 have negative Eu anomalies and an overall REE enrichment over CI chondrites by 1.4–1.8 (Lodders 2003). Note that the sample "N01 Light" is not a pure light lithology, but made of mostly dark lithologies. "N01 Ave (F)" is an averaged value of seven larger fragments obtained at Fordham.

The observed pattern is often seen in equilibrated ordinary chondrites (e.g., Haas and Haskin 1991; Friedrich et al. 2003) and has been attributed to an inhomogeneous distribution of plagioclase (carrier of positive Eu anomalies) and apatites (and pyroxene, to a lesser extent, as major REE carriers) formed during thermal metamorphism in equilibrated ordinary chondrites, with olivine, metal, and sulfide acting as diluting agents for REE concentration (Mason and Graham 1970). The melting and mobilization of plagioclase and apatites due to their low impedance to shock compression during shock events is probably limited to a scale of at most 1 mm (Fig. 7). A gram-sized sample would be required to obtain a representative sampling of Novato, given the observed heterogeneous distribution of phosphates and plagioclase (Fig. 8). Hence, compositional differences that deviate from the "chondritic norm" should be evaluated critically.

Oxygen and Chromium Isotopes

Oxygen isotopes were measured at the University of New Mexico (Table 5a). Four aliquots derived from Novato N01-2b-1 were all of the dark lithology and provided an average $\delta^{17}O = 3.67 \pm 0.102‰$, $\delta^{18}O = 4.812 \pm 0.206‰$, and $\Delta^{17}O = 1.131 \pm 0.014‰$. Four aliquots from N01-2b-15 were 50% light and 50% dark lithology and had average $\delta^{17}O = 3.654 \pm 0.034‰$, $\delta^{18}O = 4.724 \pm 0.093‰$, and $\Delta^{17}O = 1.159 \pm 0.025‰$. Three aliquots from N05-1 provided an average $\delta^{17}O = 3.804 \pm 0.090‰$, $\delta^{18}O = 5.010 \pm 0.193‰$, and $\Delta^{17}O = 1.159 \pm 0.013‰$. These values are not significantly different. Taken together, the oxygen isotope values were $\delta^{17}O = 3.701 \pm 0.098‰$, $\delta^{18}O = 4.834 \pm 0.193‰$, and $\Delta^{17}O$ 1.149 ± 0.022‰ (n = 8), respectively. These values plot in the overlapping area of the L and LL chondrite fields in Fig. 9 (Clayton et al. 1991). The distinction of Novato being L chondrite rather than LL chondrite is more apparent in the $\Delta^{17}O$ versus Fa value of olivine plot (Fig. 9B).

Further evidence for an L chondrite classification comes from the high precision $\varepsilon^{54}Cr$ isotope composition of Novato (Table 5b), which was measured for both dark and light lithologies at UC Davis, following procedures similar to that applied to pieces of the Sutter's Mill carbonaceous chondrite (cf. Jenniskens et al. 2012). Whereas the dark lithology of Novato is typical of most other ordinary chondrites, the light lithology appears to have an elevated $\varepsilon^{54}Cr$ value (Fig. 9C). We note that $\Delta^{17}O$ values for the light lithology are also higher than that of the dark lithology (Fig. 9D). This is consistent with the parallel positive trend of $\Delta^{17}O$ versus $\varepsilon^{54}Cr$ shown for carbonaceous chondrites (Fig. 9D). The underlying cause for such a trend is not well understood.

Table 4. Abundances of major, minor, and trace elements in the Novato L6 chondrite

		Orgueil (CI standard)		UC Davis HR-ICP-MS					Fordham Q-ICP-MS
		UC Davis	Reference[a]	N01 (L)	N01 (D)	N06 (L)	N06 (D)	N05 (L)	N01[c]
Li	ppm	1.56	1.47	1.03	1.01	0.89	1.75	0.72	1.6
Be	ppm	0.02	0.03	0.02	0.02	0.02	0.02	0.02[b]	
Na	wt%	0.51	0.50	0.79	0.65	0.76	0.75	0.79[b]	
Mg	wt%	9.65	9.58	14.86	12.31	12.81	15.63	14.83[b]	
Al	wt%	0.89	0.85	1.12	0.96	1.10	1.22	1.13	
P	wt%	0.12	0.10	0.11	0.14	0.07	0.13	0.09[b]	
K	wt%	0.05	0.054	0.07	0.06	0.07	0.06	0.07	
Ca	wt%	0.86	0.92	1.23	1.21	0.97	1.61	1.34[b]	
Sc	ppm	6.11	5.90	8.21	7.46	6.36	10.40	9.29	8.27
Ti	wt%	0.05	0.05	0.06	0.06	0.06	0.07	0.07[b]	0.056
V	ppm	75.9	54.3	56.1	51.2	73.6	70.8	56.4	58
Cr	ppm	2464	2650	3098	1889	3943	3319	2286	
Mn	wt%	0.18	0.19	0.27	0.23	0.23	0.29	0.27[b]	0.279
Co	ppm	503.3	506.0	544.5	316.8	1164.6	491.2	556.2[b]	540
Fe	wt%	20.29	18.50	20.67	19.79	27.52	21.97	21.52	
Ni	wt%	1.06	1.08	1.43	0.90	3.03	1.05	1.40[b]	
Cu	ppm	137	131	78.0	71.9	135	53.7	70.0	104
Zn	ppm	302	312	47.0	35.7	47.4	94.7	39.9	105
Ga	ppm	9.21	9.80	5.11	2.74	4.90	4.07	4.23	5.1
As	ppm								1.2
Se	ppm								9.6
Rb	ppm	2.34	2.31	2.58	2.04	2.47	2.57	2.37	2.5
Sr	ppm	7.16	7.81	9.34	7.75	8.64	9.21	9.35	9
Y	ppm	1.64	1.53	2.30	2.83	1.29	2.40	1.61	2.32
Zr	ppm	4.30	3.62	5.73	5.06	4.37	6.97	5.60	7.1
Nb	ppm	0.292	0.279	0.356	0.408	0.302	0.394	0.348	0.47
Mo	ppm								2.1
Ru	ppm								1.4
Ag	ppb								90
Pd	ppb								860
Cd	ppm	0.618	0.674	0.016	0.021	0.017	0.345	0.017	
Sn	ppb								370
Sb	ppm	0.160	0.130	0.083	0.052	0.140	0.066	0.093	0.11
Te	ppb								650
Cs	ppb	0.183	0.189	0.003	0.004	0.004	0.015	0.004	8
Ba	ppm	2.186	2.460	2.895	2.211	2.699	2.826	3.214	3.1
La	ppm	0.240	0.246	0.319	0.414	0.181	0.339	0.215	0.35
Ce	ppm	0.665	0.600	0.909	1.187	0.502	0.950	0.604	0.92
Pr	ppm	0.102	0.091	0.137	0.178	0.075	0.143	0.091	0.14
Nd	ppm	0.479	0.464	0.648	0.838	0.352	0.674	0.434	0.63
Sm	ppm	0.157	0.152	0.212	0.273	0.118	0.224	0.145	0.22
Eu	ppm	0.061	0.058	0.074	0.064	0.062	0.081	0.070	0.08
Gd	ppm	0.211	0.205	0.296	0.376	0.163	0.314	0.204	0.29
Tb	ppm	0.041	0.038	0.056	0.071	0.032	0.061	0.040	0.06
Dy	ppm	0.236	0.255	0.331	0.415	0.187	0.357	0.237	0.30
Ho	ppm	0.061	0.057	0.088	0.109	0.050	0.095	0.064	0.08
Er	ppm	0.166	0.163	0.240	0.295	0.140	0.261	0.181	0.22
Tm	ppm	0.026	0.026	0.036	0.043	0.022	0.040	0.028	0.04
Yb	ppm	0.158	0.169	0.219	0.255	0.135	0.242	0.181	0.22
Lu	ppm	0.026	0.025	0.037	0.041	0.023	0.041	0.031	0.04
Hf	ppm	0.098	0.106	0.137	0.123	0.104	0.172	0.140[b]	0.17
Re	ppb								60
Ta	ppm	0.019	0.015	0.023	0.024	0.021	0.028	0.024[b]	

Table 4. *Continued*. Abundances of major, minor, and trace elements in the Novato L6 chondrite.

		Orgueil (CI standard)		UC Davis HR-ICP-MS					Fordham Q-ICP-MS
		UC Davis	Reference[a]	N01 (L)	N01 (D)	N06 (L)	N06 (D)	N05 (L)	N01[c]
Ir	ppm								610
Pt	ppm								1
Tl	ppm	0.121	0.142	0.001	0.001	0.001	0.002	0.001	
Pb	ppm	2.644	2.630	0.060	0.045	0.069	0.062	0.045	
Th	ppm	0.029	0.031	0.032	0.034	0.027	0.053	0.041	0.047
U	ppm	0.008	0.008	0.006	0.005	0.013	0.017	0.050	0.014

[a]Reference values for Orgueil taken from Lodders 2003 and Lodders et al. (2009).

[b]Calibrated using terrestrial standards, BCR-2, BHVO-2, AGV-2, and JP-1.

[c]7 fragment average values. The bulk abundance of C in Novato N01 is 611.3 ppm in dark material and 97.6 ppm in light material, while that of N is 13.9 and 3.0 ppm, respectively (Table 13).

Methods: At UC Davis, approximately 10–20 mg each of clean sample fragments from Novato N01-1e-4 (light and dark lithologies, respectively), N06 (light and dark lithologies, respectively), and a pure light lithology of N05 were powdered in a clean agate mortar. Fusion crusts were carefully removed before crushing. The whole-rock powders were dissolved in concentrated 3:1 HF-HNO_3 mixture, and heated in the oven using stainless steel bombs at 190 °C for 96 h, to ensure complete dissolution of refractory phases, such as chromites. Sample dilution factors were approximately 1300 for trace element analyses and 45,000 for major element analyses, respectively. Limits of detection (3σ standard deviation of background) vary depending on the elements in question; REEs were in the ppq (10^{-15}) level, while higher blank elements such as Na, B, Ni, Cu, Zn, Mg, and Ca were 0.1–0.5 ppb. Concentrations were calculated using a calibration curve composed of a number of known meteorite standards (Murchison [CM2], Allende [CV3]), and/or a suite of terrestrial standards (BCR-2, BHVO-2, AGV-2, and JP-1). These standards were measured together with the Novato and Orgueil meteorite samples. Accuracy was assessed by comparing our Orgueil (CI1) data with those of literature values (Lodders [2003] compilation).

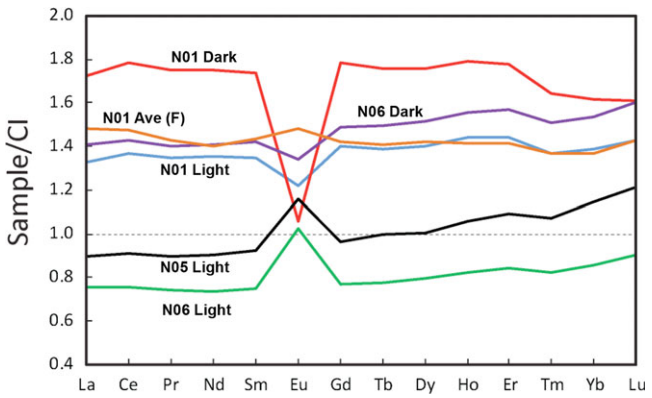

Fig. 6. CI chondrite normalized rare earth element pattern of fragments of Novato N01, N05, and N06. "Light" refers to light lithology, and "Dark" refers to dark lithology (as shown in Fig. 2). Note that the pattern designated as "N01 Ave (F)" is an average of values from seven fragments of both light and dark lithologies (all from Novato 01, mostly dark lithologies).

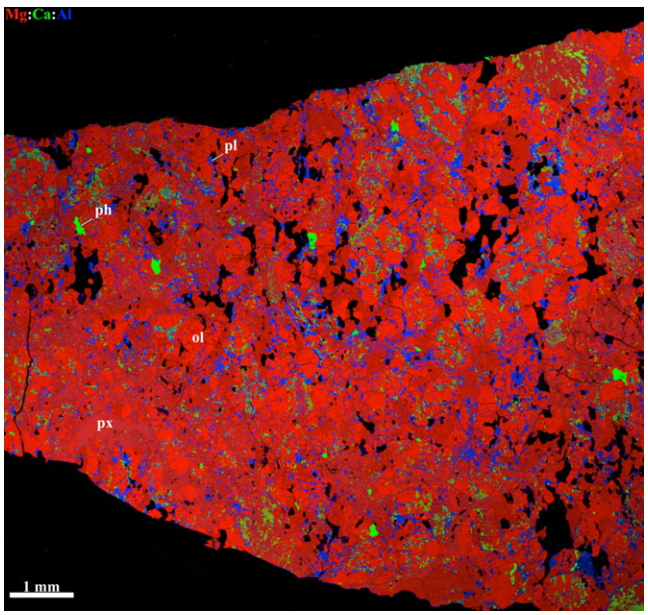

Fig. 7. Combined elemental maps of Novato N06 in Mg (red), Ca (green), and Al Kα X-rays (blue). ol = olivine; pl = plagioclase; ph = phosphate; px = low-Ca pyroxene.

CONDITIONS OF THE FALL AND PRE-ATMOSPHERIC ORBIT

The fall was exceptionally well documented. An all-sky image by James D. Wray in Foresthill captured the fireball near the horizon from a distance, providing a global view of the brighter parts. A 30 s exposed all-sky image by Wesley Jones from Belmont covered about the same early part of the trajectory as the CAMS cameras. Most of the bright part of the meteor was captured by a video security camera at Lick Observatory, focused on the near-field. The part below 42 km, including peak brightness, was captured in a series of digital still photographs by Robert P. Moreno Jr. from Santa Rosa (see below). A narrow field digital image by Phil Terzain from a location in the Santa Cruz Mountains captured the very end of the fireball against stars of the asterism of the Big Dipper. The end of the fireball was also captured in photographs by

Table 5a. Summary of oxygen isotope values for Novato.

100% dark	Mass (mg)	Date	$\delta^{17}O'$	$\delta^{18}O'$	$\delta^{17}O'$	$\Delta^{17}O'$	*n*
N01-1e-1	1.3	Dec. 12, 2012	3.688	4.856	3.688	1.124	2
N01-1e-1	1.9	Dec. 12, 2012	3.808	5.076	3.808	1.128	1
N01-1e-1	1.9	Dec. 13, 2012	3.577	4.593	3.577	1.152	2
N01-1e-1	1.8	Dec. 13, 2012	3.613	4.722	3.613	1.120	2
N01-2b-15	1.2	Dec. 12, 2012	3.695	4.813	3.695	1.154	1
N01-2b-15	2.0	Dec. 13, 2012	3.658	4.698	3.658	1.177	2
N01-2b-15	1.7	Dec. 13, 2012	3.611	4.605	3.611	1.180	2
N01-2b-15	1.7	Dec. 13, 2012	3.651	4.781	3.651	1.127	2
N05-1	1.1	Aug. 22, 2013	3.907	5.229	3.907	1.146	1
N05-1	1.7	Aug. 22, 2013	3.765	4.938	3.765	1.158	1
N05-1	1.1	Aug. 22, 2013	3.741	4.864	3.741	1.173	1

n marks the number of one set of mass spec analyses consisting of 20 cycles of standard-sample comparisons.

Table 5b. Summary of chromium isotope values for Novato, compared with mean values from other meteorites.

	Type	$\varepsilon^{53}Cr$	$\varepsilon^{54}Cr$
Novato (dark)	L6	0.23 ± 0.04	−0.37 ± 0.12
Novato (light)	L6	0.20 ± 0.04	−0.19 ± 0.13
Chainpur	LL3.4	0.24 ± 0.06[a]	−0.47 ± 0.07[b]
Chelyabinsk	LL5	0.23 ± 0.03[c]	−0.38 ± 0.08[c]
Olivenza	LL5	0.23 ± 0.06[a]	No data
Saint-Séverin	LL6	0.28 ± 0.06[a]	−0.41 ± 0.10[b]
Knyahinya	L5	0.15 ± 0.06[a]	−0.38 ± 0.08[b]
Ste.-Marguerite	H4	0.13 ± 0.06[a]	−0.39 ± 0.07[b]
Kernouvé	H6	0.19 ± 0.06[a]	−0.37 ± 0.07[b]

[a]Trinquier et al. (2008).
[b]Trinquier et al. (2007).
[c]Popova et al. (2013).

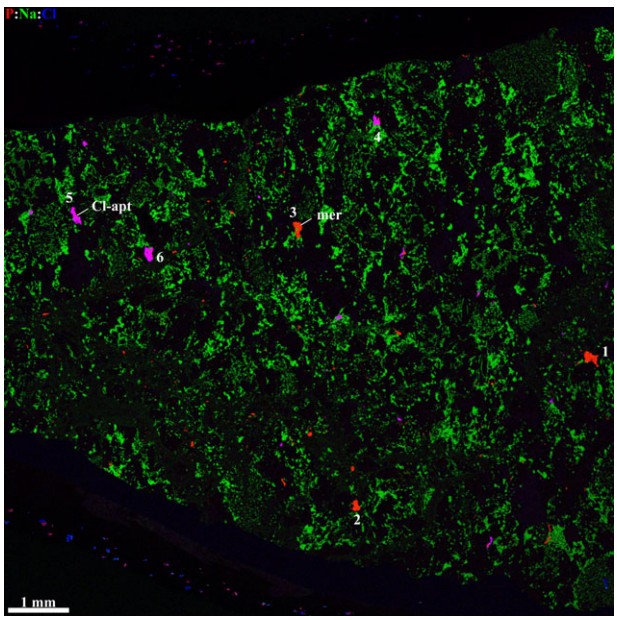

Fig. 8. Combined elemental maps of Novato N06 in P (red), Na (green), and Cl Kα X-rays (blue). Al-apt = Cl-apatite; mer = merrillite.

Rachel Fritz at Cabrillo College and by Ralph Marbach in Salinas.

Trajectory and Pre-Atmospheric Orbit

It was quite fortuitous that the fireball also traveled through the video camera fields of the CAMS project (Jenniskens et al. 2011). The goal of CAMS is to measure meteoroid trajectories by triangulation of +4 magnitude meteors and brighter, to map meteor showers throughout the year. The project consists of three stations, each equipped with 20 Watec Wat 902H2 Ultimate low-light level video security cameras with 20° × 30° field of view pointed at different directions in the sky so that all elevations above 30° are covered. The stations are located at Fremont Peak Observatory, Lick Observatory, and in Sunnyvale, CA. In addition, single cameras with the same specifications are operated by participating amateur astronomers at several other locations in the San Francisco Bay area.

Five CAMS cameras filmed the first 11.1 s of the meteor from three locations, starting at 02:44:29.9 ± 0.7 UT on 18 October (Fig. 10). The Lick Observatory station captured the beginning of the meteor in camera #164. It then emerged behind a tree at the Sunnyvale station, where it was tracked by three video cameras (#152, #51, and #11, respectively). The final part was also captured by the single camera #210 of the College of San Mateo station.

To keep the astrometric precision high, each 8 seconds of video is compressed in four frames that contain the peak, average, and standard deviation of brightness at each pixel and the frame number in which peak brightness occurred (Jenniskens et al. 2011). The reconstructed video shows a point-like meteor image in cameras 164 and 152, but a speckled disk due to blooming in later cameras. The centroid of each image was carefully determined and while the centroid may be off-center due to optical distortions, the meteor's path is

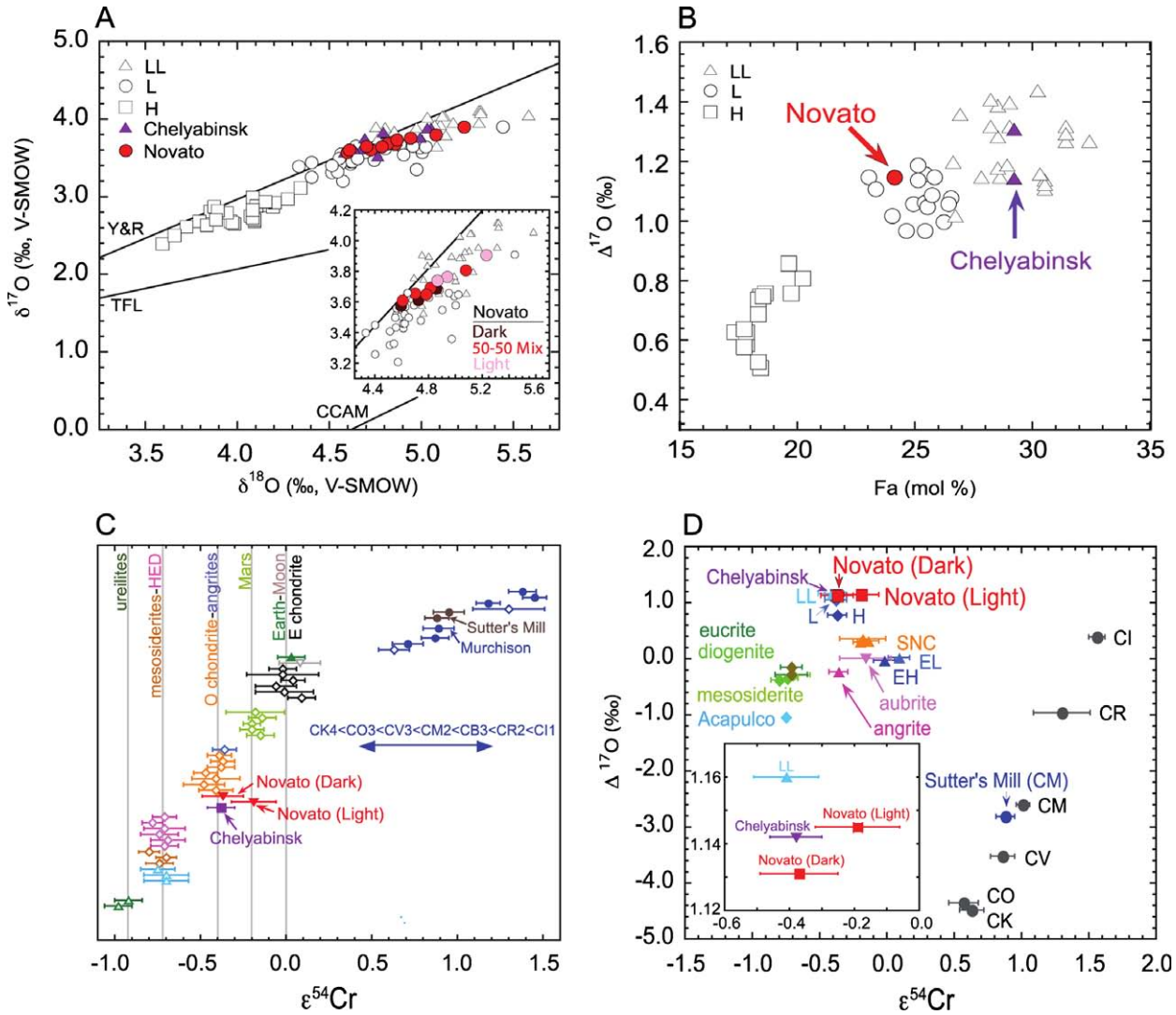

Fig. 9. A) Three oxygen-isotope diagram, showing Novato data together with H, L, and LL chondrites (Clayton et al. 1991). The inset shows the L and LL chondrite regions with the Novato data in more detail. B) $\Delta^{17}O$ versus Fa mol% of olivine in Novato, compared with other ordinary chondrites groups—H, L, and LL (data source: Troiano et al. [2011] and references therein). C) Variation of $\varepsilon^{54}Cr$ values among the various extraterrestrial materials. Novato dark lithology is identical to those of reported values for ordinary chondrites, whereas the light lithology of Novato shows a higher value, consistent with the higher $\Delta^{17}O$ value for the light lithology (Table 5, and panel D inset). Filled symbols represent data acquired at UC Davis. Open symbols are literature data: diamonds, inverted triangle, and regular triangles are from Trinquier et al. (2007), Qin et al. (2010), and Yamakawa et al. (2010). D) $\varepsilon^{54}Cr$ versus $\Delta^{17}O$ for Novato, compared with the other major meteorite groups. Data sources for $\Delta^{17}O$ and $\varepsilon^{54}Cr$ are from Clayton and Mayeda (1984, 1996, 1999), Clayton et al. (1991), Young and Russell (1998), Jenniskens et al. (2012), Trinquier et al. (2007), Göpel and Birck (2010), and Irving et al. (2011). Chelyabinsk data shown for comparison in all four panels are from Popova et al. (2013). Notes: TFL refers to the terrestrial mass-dependent fractionation line; CCAM refers to carbonaceous chondrite anhydrous mineral line (Clayton and Mayeda 1999); Y&R refers a slope of 1 line defined by unaltered minerals from CV CAIs by Young and Russell (1998). Fa mol% is defined as mole ratio of Fe/(Fe+Mg) in olivine; $\Delta^{17}O$ is the deviation from the terrestrial fractionation line following the relationship $\Delta^{17}O = \delta^{17}O' - 0.528 \times \delta^{18}O'$, where $\delta^{17,18}O' = \ln(\delta^{17,18}O/10^3 + 1) \times 10^3$, $\delta^{17,18}O = ([^{17,18}O/^{16}O]_{sample}/[^{17,18}O/^{16}O]_{SMOW} - 1) \times 10^3$, and SMOW refers to standard mean ocean water.

well recorded in the average image due to integration of the more persistent fireball's wake. The time-averaged frame preserves this wake plus a rich ($N > 100$) star field, which is used for astrometry (e.g., (b) in Fig. 10). The calculated centroid was projected onto the meteor path defined by the wake.

The trajectory was calculated using methods described in Jenniskens et al. (2011). Figure 11 shows

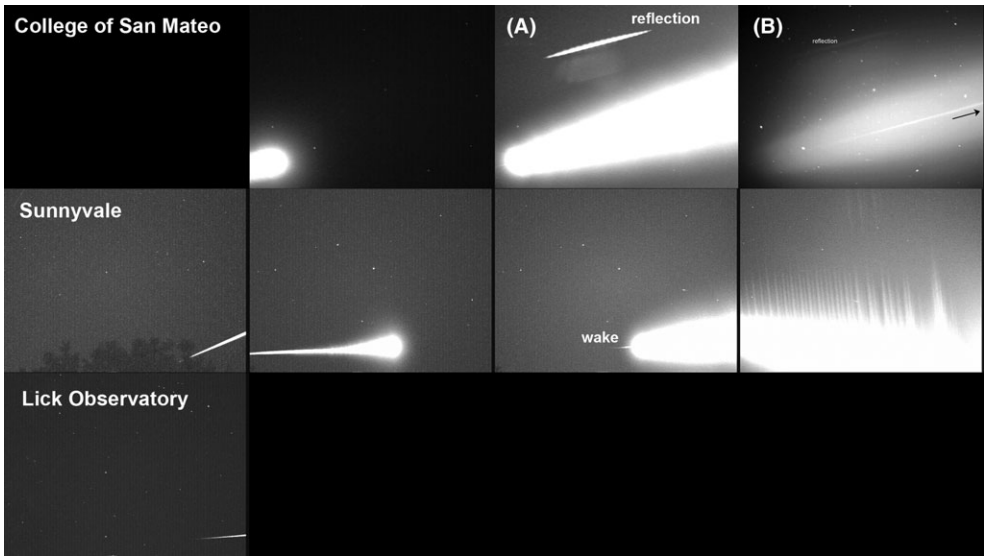

Fig. 10. Cameras for Allsky Meteor Surveillance detections of the November 17 fireball shown as the maximum pixel intensity for each pixel over an 8 s video sequence. A) College of San Mateo maximum pixel image. B) Same, but time-average data over the same time interval.

the trajectory solutions from combining the first 2, 3, 4, and 5 cameras. The 2-camera solution is hampered by a small convergence angle (Q) and large distance from meteor to stations. Solutions with 3 or 4 cameras converge on a solution that aligns with the majority of Novato meteorite finds ($Q = 9.5°$), labeled N02 to N06 in Fig. 11. The solutions that include the bloomed video of cameras 11 and 51 ($Q = 21.4°$) tend to produce slightly lower velocities and align closer to the N01 find, passing about 0.7 km east of it (Fig. 11).

The five-camera solution's observed minus calculated (O−C) values for azimuth and elevation of the meteor in each video frame are shown in Fig. 12. The observed position of the meteoroid rarely deviates by more than ±0.1° (about 2 pixels) from the calculated position.

The remaining deviations in Fig. 12 are due to systematic differences between the measured centroid of the bloomed image and the actual meteoroid position. Because the centroid positions were projected onto the meteoroid wake, the random uncertainty in elevation is significantly smaller than that in azimuth.

Because the deceleration is so small above 46 km, a different choice for the deceleration profile does not much improve O-C. Fitting a deceleration curve described in Jenniskens et al. (2011) results in an apparent entry speed of $V_\infty = 13.672 \pm 0.013$ km s^{-1} and a small value for the deceleration parameter $a_1 = 6.7 \pm 4.0 \times 10^{-8}$ km (and $a_2 = 1.43 \pm 0.10$/s). A constant velocity fit has $V_\infty = 13.555 \pm 0.008$ km s^{-1}. The much higher uncertainty intervals given in Table 6a include systematic uncertainties by covering all these reasonable deceleration solutions.

Using the Schiaparelli equation to approximate the influence of Earth's gravity on the orbit (column A in Table 6b) results in an orbit that is defined as Earth not being at that location. Such an approximate orbit is not suitable for backward integrations. To create a suitable description of the pre-atmospheric orbit, 1000 meteoroid clones were generated using Gaussian distributions over the atmospheric contact position and velocity uncertainties noted in Table 6a. Each clone in this probability cloud was integrated back in time using a RADAU integrator (Everhart 1985; Clark and Wiegert 2011) accounting for gravitational influences of the Sun, major planets, and the Moon. Integrating backward results in the orbital elements listed in column B of Table 6b.

Light Curve and Initial Mass

The photometric lightcurve is shown in Fig. 13. CAMS cameras recorded the fireball down to 46 km altitude. Moments later, a set of two bright flares light up the sky just outside the field of view. The video security camera at Lick Observatory captured most of this bright part of the meteor, including the flares around peak brightness. The all-sky image from Foresthill provides a global view, while the photographs from Santa Rosa provide a light curve for the later part of the trajectory.

The sum pixel intensities of the meteor images in the un-intensified video frames and individual digital still photographs were corrected for saturation using a blooming correction $I_o' = I_o \exp(I_o/\tau)$, where τ is a free parameter, which specifies at what sum pixel intensity

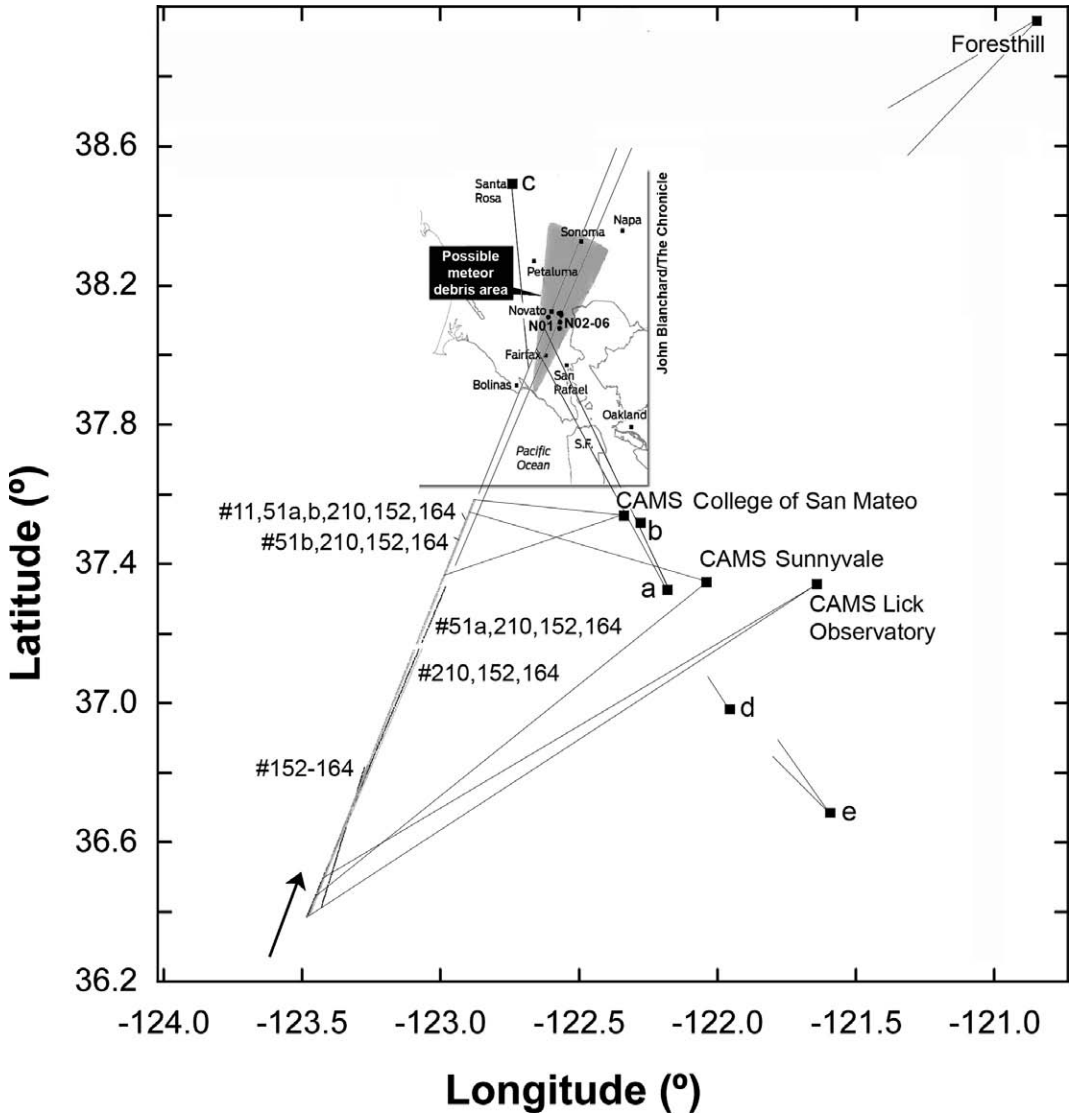

Fig. 11. Trajectory solutions derived from different combinations of cameras (identified by their number) and the station locations, including (a) Phil Terzain, (b) Wesley Jones, (c) Robert P. Moreno Jr., (d) Rachel Fritz, and (e) Ralph Marbach. Also shown are the locations of the recovered meteorites (N01, N02–N06) and a reproduction of the possible fall area published in the San Francisco Chronicle based on early Cameras for Allsky Meteor Surveillance (CAMS) results (gray area).

the signal starts to saturate. CAMS data were scaled using the previously determined τ value (Jenniskens et al. 2011). The relevant value for the free parameter of other data sets was determined by scaling data to the low-intensity parts of other cameras. This blooming correction was found to be satisfactory for the un-intensified CCD imagers in low-light video and digital still cameras during past data analysis (Jenniskens 2010).

Because of saturation in all images, the lightcurve's peak brightness is uncertain by at least one visual magnitude. A visual peak brightness of -13.8 ± 1.0 magnitude (as seen from a distance of 100 km) and effective duration of 1.96 ± 0.09 s (= the integrated brightness profile/peak brightness) would correspond to a total radiated energy emitted at optical wavelengths (400–700 nm) of 9×10^8 J ($4–22 \times 10^8$ J), and this translates to a kinetic energy of 1×10^{10} J ($0.5–3 \times 10^{10}$ J) or 3 tons of TNT (1–8 tons of TNT) for a luminous efficiency of 7% (Revelle and Ceplecha 2001). This would correspond to a meteoroid diameter of 43 ± 13 cm and a mass of 135 (50–340) kg, if the meteoroid had the same density as the recovered meteorites.

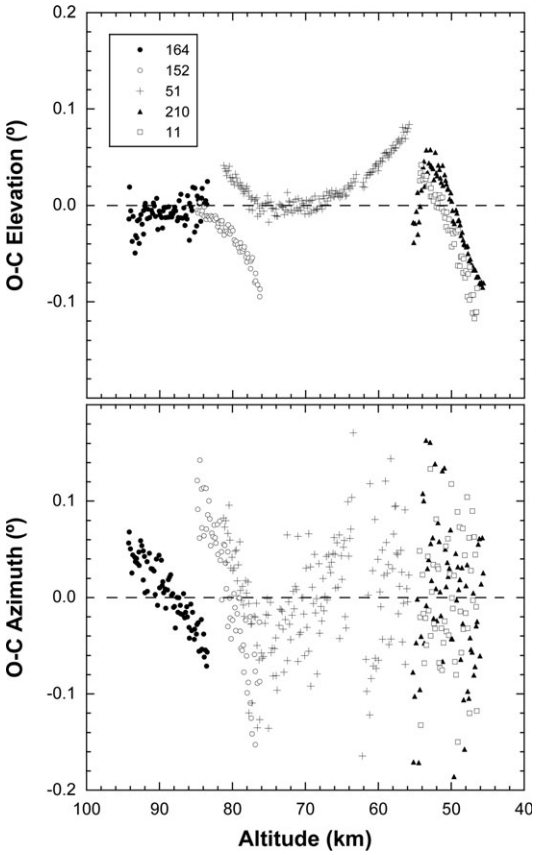

Fig. 12. Observed minus calculated values for azimuth and elevation of the meteor in all video frames, with data from individual camera fields separately labeled. One video frame pixel equals 0.047° in elevation and about 0.06° in azimuth.

Dark Flight and Source Energy

Based on upper atmosphere wind sounding data from station 72493 OAK in Oakland at 0 h UT on October 18 (http://weather.uwyo.edu/upperair/sounding.html), prevailing winds below 30 km were blowing predominantly from the west over much of the dark flight trajectory, gradually changing to a more northerly and northeasterly direction below 9 km. So, meteorites would have fallen just east of the calculated trajectory, but only by about 430 m perpendicular to the trajectory for a 100 g meteorite and 120 m for a 1 kg meteorite (sphere, density 3.3 g cm^{-3}, fall from 43 km altitude, and drag coefficient $C_d = 0.43$ for Mach number Ma <0.5, $C_d = 1.00$ for Ma >1.4, and $C_d = 0.715 + 0.285$ sin [3.1415 (Ma/0.9–1.05) rad.] in between). A 61.9 g stone would have hit the Webber residence at 54 m s^{-1} after having broken off at about 35 km altitude.

The falling meteorites may have been detected by the nearest Doppler weather radar KMUX—San Francisco (37.1550°N, 121.8978°W) for elevation 3.62° at 2:39:44 UT (Fig. 14). Multiple returns were located over Marin County where meteorites of approximately 1–10 g were expected to fall. This is a similar size range as thought to have been responsible for the Sutter's Mill radar return signal (Jenniskens et al. 2012). Some signal was also detected over Novato (Fig. 14), possibly reflecting the ongoing fragmentation of the meteorites (Fig. 15).

Audible sounds were reported in Marin County. Low-frequency sound waves emanating from the

Table 6a. Novato trajectory from all Cameras for Allsky Meteor Surveillance (CAMS) data above 45.6 km altitude (cameras 11, 51, 152, 164, and 210). End height and position are for the last observed point.

Parameter	Novato (all CAMS cameras)
Date (y-m-d)	2012-10-18
Time start, UTC (h:m:s)	02:44:29.88 ± 0.7
Begin Julian Date Ephem.	2456218.615
α_R (°)	280.98 ± 0.15
δ_R (°)	−30.65 ± 0.15
V_∞ (km s^{-1})	13.67 ± 0.12
Radiant azimuth from S at start (°)	21.48 ± 0.18
Radiant elevation at start (°)	19.37 ± 0.10
H start (km)	94.4 ± 0.3
Longitude start (°)	236.537 ± 0.005
Latitude start (°)	+36.395 ± 0.003
H end (km)	<45.72 ± 0.05
V end (km s^{-1})	<13.38 ± 0.29
Longitude end (°)	>237.126 ± 0.001
Latitude end (°)	>+37.584 ± 0.002
Convergence angle (°)	21.4

Table 6b. Overview of Novato orbit determinations (Equinox J2000). Solution (A) used the Schiaparelli's equation for correction from apparent to geocentric reference frame, while solution (B) integrated the orbit to a moment 2 months before impact.

Parameter	Novato (A) Schiaparelli	Novato (B) Integrated orbit −2 months
Solar longitude	204.9669 ± 0.0001	204.9669 ± 0.0001
α_G (°)	268.1 ± 0.6	–
δ_G (°)	−48.9 ± 0.7	–
V_G (km s^{-1})	8.21 ± 0.22	–
Epoch (TD)	–	2456158.615012
a (AU)	2.09 ± 0.11	2.088 ± 0.077
q (AU)	0.9880 ± 0.0003	0.9880 ± 0.0001
e	0.526 ± 0.024	0.526 ± 0.017
i (°)	5.5 ± 0.6	5.508 ± 0.040
ω (°)	347.37 ± 0.18	347.352 ± 0.134
Node (°)	24.9414 ± 0.0005	24.9900 ± 0.0035
M (°)	–	343.702 ± 0.851

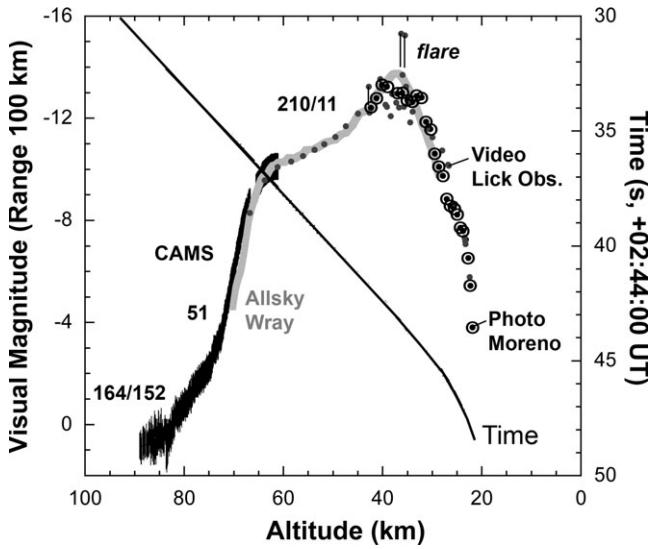

Fig. 13. Novato fireball visual brightness as seen from a distance of 100 km, and the approximate deceleration profile. Video data are from Cameras for Allsky Meteor Surveillance (CAMS) (cameras ##164, 152, 51, 210, and 11) and from a video security camera at Lick Observatory, an allsky image by James D. Wray (solid line), and a series of photographs by Robert P. Moreno Jr. The position of flares in the Lick video is marked by vertical lines.

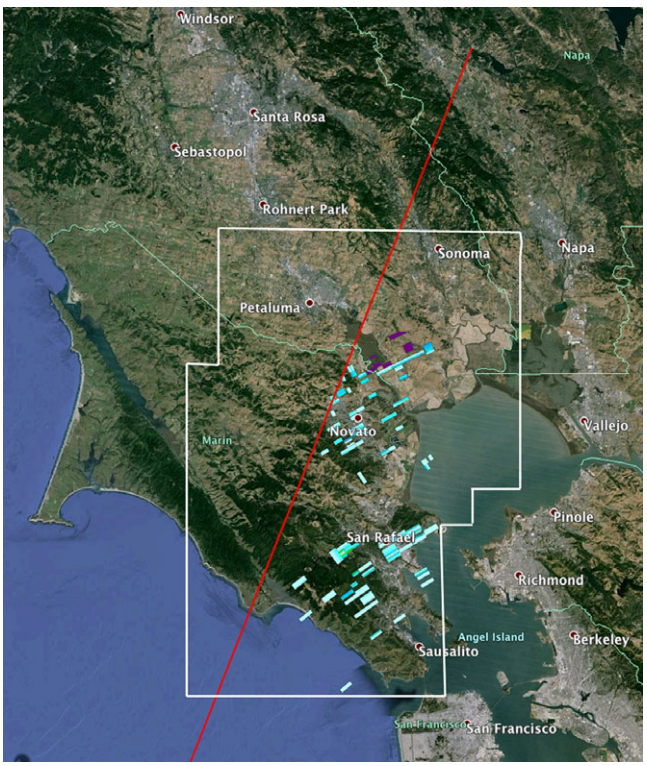

Fig. 14. Doppler weather radar returns (KMUX 2:39:44 UT) that may derive from falling meteorites and location of the trajectory in Marin, Napa, and Sonoma counties.

Table 7. Summary of the infrasound signal measurements as recorded by I57US, located 310 km from the fireball trajectory terminal point.

	Arrival 1	Arrival 2
Arrival time (UT)	3:25:02	3:26:00
Delay time (s)	2348	2452
Celerity (km s^{-1})	0.311	0.303
Max. amplitude (Pa)	0.012 ± 0.005	0.039 ± 0.010
Max peak-to-peak amplitude (Pa)	0.020 ± 0.011	0.054 ± 0.020
Period of maximum amplitude (s)	0.7 ± 0.0	0.6 ± 0.1
Frequency at maximum PDS (Hz)	1.48	1.58
Period at maximum PSD (s)	0.7	0.6
Total duration (s)	45	90
Trace velocity (km s^{-1})	0.363	0.363
Observed back azimuth (°)	309.6	309.6

Novato fireball were detected at I57US (+33.6058°N, 116.4532°W), the closest of five infrasonic stations of the International Monitoring System (Christie and Campus 2010). Located just over 300 km from the event, two arrivals were detected that are consistent with the propagation timing of a typical fireball at such ranges. Utilizing the standard method of cross-correlating the output between each sensor and performing beam forming of the signals across the array (Evers and Haak 2001), the arrival azimuth corresponds to the predicted azimuth associated with the fireball. Table 7 summarizes the properties of both signal arrivals recorded by I57US. The blast wave coupled to the ground and created a weak seismic signature at 37 seismic stations located within a 100 km radius, with an origin centered at 10 km altitude above lat. = +37.92°N, long. = 122.60°W (origin time at 02:45:20 UT), near Mount Tamalpais. No seismic signal from impacting meteorites was detected on high-resolution three-component borehole strain and seismic instrumentation near Novato and Sonoma.

The infrasound records provide a measure of the source energy, which is derived using several empirical relations. These employ either the period at maximum amplitude or the range and signal amplitude (Ens et al. 2012). Both the dominant period and high frequency content of the signal clearly point to a low-energy source. The yield estimate, based on both of these methodologies, is several tons of TNT equivalent (with the lower range of 1 *t*, and the upper range of approximately 10 tons). That would put the pre-atmospheric mass between 45 and 450 kg (nominally 140 kg) and the diameter (if a sphere, using the measured density of 3.3 g cm^{-3}) at around 30–60 cm (nominally 40 cm).

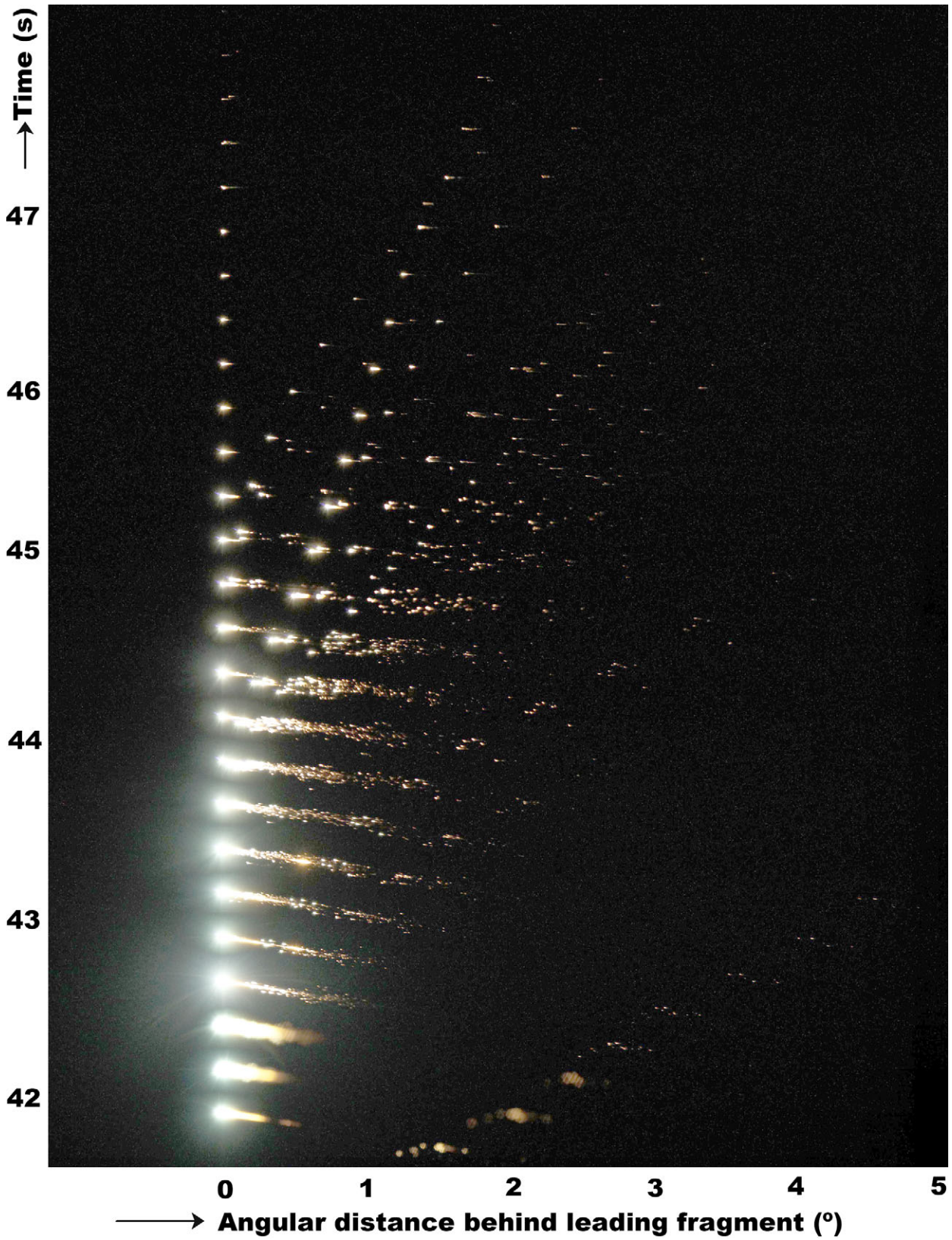

Fig. 15. Fragmentation and relative deceleration at the end of the trajectory in a compilation of digital photographs of the October 17, 2012, fireball by Robert P. Moreno Jr. of Santa Rosa. Photographs were taken at a rate of 4 per second with a Canon EOS 7D camera set at 200 mm focal length and F2.8 diaphragm, with 1/320 s exposure time at ISO 1600.

Fragmentation

The meteoroid fragmentation was well documented in a particularly nice set of photographs obtained with a hand-held Canon EOS 7D camera by Robert P. Moreno Jr. in Santa Rosa while at a sporting event at the Cardinal Newman High School (for location see Fig. 11). Digital still images at 18 megapixel (5184 × 3456 pixel) size were taken at a rate of 4 per second during the final 6.2 s, when the train of fragments was descending from 42 to 22 km. This covers the period of peak brightness (Fig. 13). Only two stars (ψ and ω Cap) are identified in the images.

Figure 15 shows the position of individual fragments relative to the leading fragment. This represents one of the best documents of meteoroid atmospheric fragmentations ever obtained. There were several discrete episodes of breakup. The first train of fragments was created just before the first picture was taken. Comparing to Fig. 13 shows that this first event was coincident with the first flare seen in the Lick Observatory security camera footage. In the same way, the later set of two flares seen in rapid succession at peak brightness (Fig. 13) coincides with the origin of the two most prominent debris trains seen later on in Fig. 15.

Most of the mass (M) in each fragment train is in the largest (brightest) pieces, the overall mass distribution being log ΣM approximately log M. Because the luminous efficiency is unknown under these ablation conditions, the surviving mass of the brighter fragments in each debris train can only be estimated at approximately 100 g based on the recovered meteorites. The initial breakup dictates the fragment size distribution in each train and the relative velocity of the debris train to that of the leading fragment. There is no sign of increasing deceleration with ongoing ablation, implying that ablation does not rapidly change the surface-to-mass ratio of the fragments. Just before fading, many fragments further break apart. This behavior differs in detail with the continuous cascading process that is often assumed in meteoroid fragmentation models (e.g., ReVelle 2002; Brown et al. 2004). The leading fragment of Novato showed the same behavior, fragmenting at the very end before fading. Hence, it is likely that no 10 kg-sized fragments landed on the ground.

Ablation

Ablation proceeded differently for light and dark materials. A close examination of the exterior of the Novato N01 and N06 stones shows a fine distribution of tiny patches of fusion crust over most of its shock-darkened surface (Fig. 1). Those patches show layers (Figs. 16A and 16B), suggesting discontinuous ablation. In contrast, centered on the light lithology of Novato N04 is a well-defined approximately 2 × 2 cm-wide fusion crust patch (Fig. 1). A smaller but similar patch is visible on the light fraction of N03 (Fig. 1). The missing fusion crust on the dark material was not lost during impact. Only a few tiny fragments of N03, no fusion crust, were found when the road was systematically searched with a magnet.

Both types of fusion crust were derived locally from the melting of the immediate, underlying lithology, with no evidence of mixing of these different melts prior to the crust solidifying. The patches of fusion crust in contact with the light chondritic material are thicker and look more similar to the fusion crust seen on other fresh chondrites (e.g., Sears 1978; p. 34–38; Brown et al. 2004), the thickness caused in part by materials with higher melting points withstanding the heating process longer (Sears and Mills 1973; Schneider et al. 2000). In contrast, the smaller patches of fusion crust in contact with the black, shock-darkened lithology appear to have been more viscous before they solidified (Figs. 16A and 16B). These melts appear to have had more difficulty adhering to that portion of the meteorite due to the lack of low melting point phases (like metal-sulfide eutectics) and the low porosity of the underlying lithology.

Spallation

Spallation played a role in the ablative process. One side of Novato N03 displays a 1–2 mm deep depression with sharp, vertical edges (Figs. 16C and 16D). A thin flake of shock-darkened material, 3 × 2 × 0.1–0.2 cm, detached itself from the stone immediately prior to the stone's entering dark flight. Submillimeter patches of fusion crust are visible on the exposed surface. As the stone is well-rounded, with traces of fusion crust on all sides, it can be assumed that mechanical spallation occurred while the meteorite was still in ablative flight. Only approximately 5% of its surface was retained long enough to leave well-developed primary fusion crust.

The brittle dark shock-hardened and troilite vein riddled chondritic material may be more susceptible to fracturing caused by high thermal gradients. The thermal gradient experienced by the outer 3 mm of a stony meteorite can reach 5000 K cm^{-1} (Ceplecha et al. 1998).

Pre-entry fractures did not cause the spallation. Novato N03 contained no such fractures, even after it had been run over numerous times by automobiles; it was found sitting amongst approximately 25 fresh

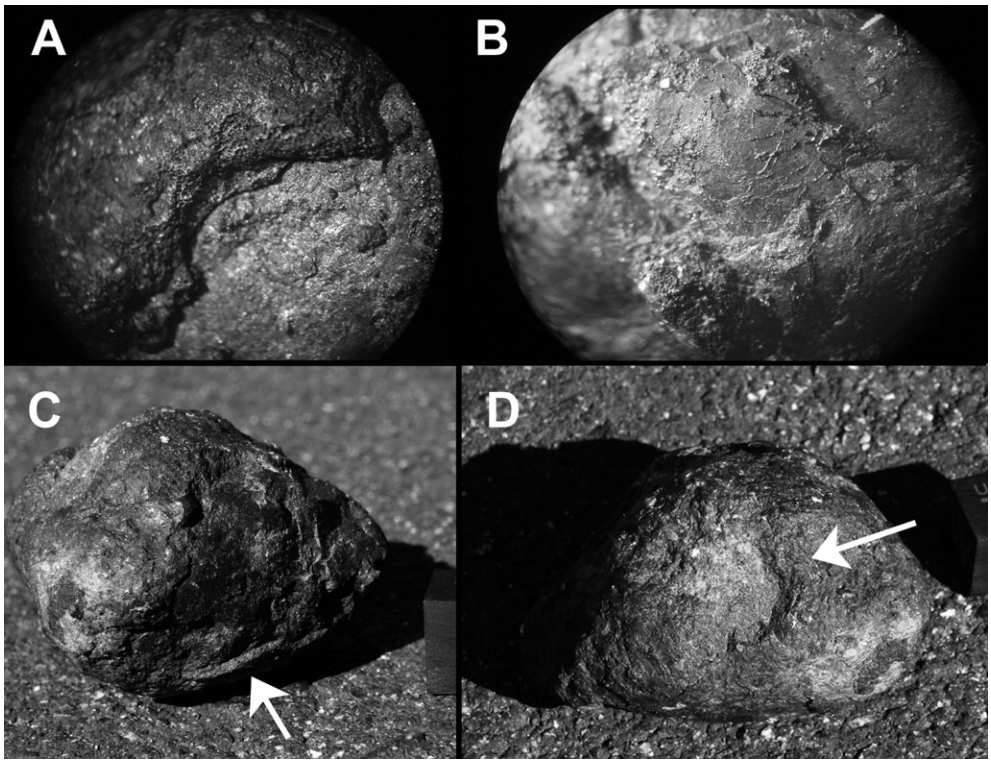

Fig. 16. A, B) Details of the fusion crust of N01, showing an area about 1 cm across. C, D) Evidence for spallation in Novato N03, showing two sides of the meteorite as it was found. Cube is 1 cm sized.

divots in the paved road where it was found. White marks from small amounts of crushed road surface were visible on all sides of the meteorite. Had the stone been internally fractured, it would have fragmented from this maltreatment. Instead, < 1 g of fragments was found in the road, mostly as a single chip approximately 5 m from the stone that does not match the depression.

Spallation as a significant contributor to meteoroid mass loss has been seldom noted in literature, except in the case of carbonaceous chondrites, where it was equated with meteoroid porosity (Baldwin and Sheaffer 1971). Spallation of fragments with a diameter less than 1/10th of that of the meteoroid can increase the ablating surface area by a factor of ten, if spallation is occurring at a mass loss rate rivaling that of ablation. Theoretical models of the lightcurve and deceleration of the Park Forest meteoroid, another equilibrated chondrite that could have undergone mechanical spallation, suggested a 40% initial porosity (Brown et al. 2004). In contrast, the recovered meteorite fragments' observed average porosity was <5%. Subsequent work revisited the luminous efficiency for given mass loss and estimated the meteoroid porosity at only 20%, corresponding to a approximately 50% lower mass (ReVelle 2007). Rapid late-stage or continuous mechanical surface spallation of otherwise intact fragments, as observed for Novato, could account for the anomalous luminous efficiency of Park Forest.

THE METEOROID IN SPACE

To determine the pre-atmospheric size of the meteoroid and its cosmic-ray exposure (CRE) age, we measured the concentrations of cosmogenic radionuclides and noble gases in sample N01. The short-lived radionuclides were measured in the whole stone (60.1 g after removal of a 1.8 g fragment for petrography) using nondestructive gamma-ray spectroscopy with a 518 cm^3 high-purity germanium detector in the STELLA (SubTErranean LowLevel Assay) facility at the Laboratori Nazionali del Gran Sasso (LNGS) in Italy (Arpesella 1996). The specimen was measured 21 days after the fall, for a period of 8.5 days: short-lived radionuclides such as ^{52}Mn (half-life = 5.9 days), ^{48}V (half-life = 16 days), and ^{51}Cr (half-life = 27.7 days) were counted. Table 8a shows the measured activities of cosmogenic radionuclides, corrected to the date of fall, while Table 8b shows concentrations of K, U, and Th based on measured activities of natural ^{40}K, ^{238}U, and ^{232}Th.

Table 8a. Massic activities (corrected to the time of fall) of cosmogenic radionuclides (in dpm kg^{-1}) in the 60.1 g specimen of the Novato L6 chondrite (N01) measured by nondestructive gamma-ray spectroscopy. Errors include a 1σ uncertainty of approximately 10% in the detector efficiency calibration. The counting efficiencies were calculated using a Monte Carlo code. This code is validated through measurements and analyses of samples of well-known radionuclide activities and geometries. The average density and composition were taken from Britt and Consolmagno (2003) and Jarosewich (1990), respectively.

Nuclide	Half-life	Activity
^{52}Mn	5.591 days	20 ± 9
^{48}V	16.0 days	20 ± 3
^{51}Cr	27.7 days	35 ± 7
^{7}Be	53.1 days	81 ± 12
^{58}Co	70.9 days	9 ± 1
^{56}Co	77.3 days	6 ± 1
^{46}Sc	83.8 days	9 ± 1
^{57}Co	271.8 days	14 ± 2
^{54}Mn	312.3 days	104 ± 11
^{22}Na	2.60 yr	108 ± 10
^{60}Co	5.27 yr	<1.4
^{44}Ti	60 yr	<2.8
^{26}Al	7.05×10^5 yr	61.1 ± 5.4

Table 8b. Concentrations of U, Th, and K (ng g^{-1} for U and Th and in μg g^{-1} for K) in the 60.1 g specimen of the Novato L6 chondrite based on the measured activities of their long-lived radioactive isotopes measured by nondestructive gamma-ray spectroscopy. Errors include a 1σ uncertainty of approximately 10% in the detector efficiency calibration.

Element	Concentration
U (ppb)	13 ± 2
Th (ppb)	44 ± 5
K (ppm)	901 ± 92

We also dissolved a 90 mg aliquot of N01 for the analysis of long-lived cosmogenic radionuclides ^{10}Be ($t_{1/2}$ = 1.36×10^6 a) and ^{26}Al (7.05×10^5 a) by accelerator mass spectrometry (AMS) at PRIME Lab (Sharma et al. 2000). The measured values were normalized to ^{10}Be and ^{26}Al AMS standards (Nishiizumi 2004; Nishiizumi et al. 2007), yielding ^{10}Be = 19.1 ± 0.5 dpm kg^{-1} and ^{26}Al = 51.4 ± 2.2 dpm kg^{-1}. The ^{26}Al AMS result is approximately 15% lower than the value of 61.1 ± 5.4 dpm kg^{-1} measured by γ-ray spectrometry (Table 8a), but overlaps within 2σ uncertainty.

Noble gases (He–Xe) were measured in five aliquots of N01 at ETH Zürich. Two samples, N01-2b-7 and N01-2b-14, taken from the same chip that was used for the ^{10}Be and ^{26}Al analysis, were measured for He, Ne, and Ar using methods described in Wieler et al. (1989) and Meier et al. (2012). The former consisted exclusively of the light lithology, while the latter was a mixture of about 70% dark and 30% light. Three more samples, N01-2b-x (light lithology), N01-2b-y (dark), and N01-2b-3 (approximately 90% dark), have been measured (as five fragments) for He–Xe in Zurich, but mainly to determine the trapped Kr and Xe content. These measurements were based on an established protocol described by Wieler et al. (1989) and Busemann et al. (2000). Results are shown in Table 9.

Meteoroid Diameter

To constrain the pre-atmospheric size, we compare the radionuclide concentrations with production rates from model calculations, based on a constant galactic cosmic ray flux. The production rates of radionuclides with half-lives of <11 yr are affected by solar activity, which modulates the galactic cosmic ray flux by up to a factor of two within a solar cycle. The fall of the Novato L6 chondrite occurred during the end of a solar minimum that preceded the current solar cycle 24. The galactic cosmic ray flux was therefore still high in the 6 yr before the fall. Indeed, the ^{22}Na/^{26}Al ratio of 1.77 ± 0.23 in Novato is on the high end of the range observed for other chondrites (Evans et al. 1982; Bhandari et al. 2002).

Of the various cosmogenic radionuclides measured, ^{60}Co is the most sensitive to pre-atmospheric size and depth, as it is produced by capture of low-energy secondary neutrons. The absence of ^{60}Co in Novato, for which only an upper limit of 1.4 dpm kg^{-1} was determined, indicates that N01 was either part of a meteoroid with a radius <20 cm, or was located very close to the surface of a meteoroid with a radius >20 cm, although the absence of ^{60}Co becomes less likely with increasing size of the object (Spergel et al. 1986). Comparison of the other radionuclide concentrations, including ^{10}Be, ^{26}Al ^{22}Na, and ^{54}Mn, with model calculations (Kohman and Bender 1967; Bhandari et al. 1993; Leya and Masarik 2009) shows that they are consistent with a radius of 15–20 cm, although they can also be explained by near surface irradiation in objects with radii up to 70–100 cm. Combining ^{60}Co with ^{10}Be or ^{26}Al, we can constrain the pre-atmospheric radius of Novato to 15–20 cm, while sample N01 was at a depth of 5–10 cm. Assuming a spherical meteoroid and a density of 3.5 g cm^{-3}, a diameter of 30–40 cm corresponds to a

Table 9a. Noble gas (He, Ne, Ar) analysis of two samples, 22.8 mg of N01-2b-7 and 47.8 mg of N01-2b-14.

#	Mass	$^{3}He/^{4}He$	^{4}He	$^{20}Ne/^{22}Ne$	$^{21}Ne/^{22}Ne$	^{22}Ne	$^{36}Ar/^{38}Ar$	$^{40}Ar/^{36}Ar$	^{36}Ar
2b-7	22.80 ± 0.05	0.0748 ± 0.0001	130.0 ± 0.3	0.894 ± 0.005	0.918 ± 0.004	2.75 ± 0.01	2.98 ± 0.01	424 ± 1	1.69 ± 0.006
2b-14	47.80 ± 0.10	0.0621 ± 0.00009	150.0 ± 0.3	0.913 ± 0.003	0.918 ± 0.03	2.69 ± 0.008	0.583[a]	611[a]	n.d.
Light small	2.52 ± 0.010	0.0833 ± 0.0013	123 ± 2	0.87 ± 0.18	0.927 ± 0.017	2.9 ± 0.8	2.0 ± 0.8		0.9 ± 0.3
Light	16.16 ± 0.02	0.0906 ± 0.0005	107.8 ± 0.4	0.864 ± 0.009	0.9214 ± 0.0026	2.58 ± 0.04	1.215 ± 0.012	477 ± 16	0.417 ± 0.003
Dark small	2.31 ± 0.010	0.0774 ± 0.0013	131 ± 2	0.75 ± 0.21	0.933 ± 0.020	2.7 ± 1.1	1.6 ± 0.8	1659 ± 772	0.8 ± 0.3
90% dark	18.50 ± 0.10	0.0686 ± 0.0006	141.5 ± 0.9	0.891 ± 0.008	0.907 ± 0.003	2.66 ± 0.04	2.903 ± 0.019	470 ± 11	1.544 ± 0.009
Dark	18.47 ± 0.01	0.0449 ± 0.0002	228.8 ± 0.5	0.878 ± 0.007	0.9104 ± 0.0023	2.71 ± 0.03	2.503 ± 0.019	1042 ± 27	1.014 ± 0.005

	$^{3}He_{cos}$	$^{21}Ne_{cos}$	$^{38}Ar_{cos}$	$3/21_{cos}$	$22/21_{cos}$	T3[b]	T21[b]	T38[b]	He-loss (%)
2b-7	9.69 ± 0.03	2.52 ± 0.33	0.284 ± 0.003	3.84 ± 0.51	1.09 ± 0.005	4.93	6.45	5.91	20
2b-14	9.34 ± 0.02	2.47 ± 0.32	n.d.	3.78 ± 0.49	1.09 ± 0.003	4.76	6.32	n.d.	25
Light small	10.27 ± 0.06	2.67 ± 0.07	0.33 ± 0.17	3.85 ± 0.10	1.079 ± 0.020	5.23 [6.31]	6.81 [6.92]	(6.83) ([6.79])	23
Light	9.77 ± 0.04	2.376 ± 0.010	0.312 ± 0.005	4.110 ± 0.024	1.085 ± 0.003	4.98 [6.02]	6.07 6.36]	6.48 [6.50]	21
Dark small	10.16 ± 0.06	2.56 ± 0.08	0.40 ± 0.26	3.97 ± 0.12	1.072 ± 0.023	5.17 [6.23]	6.53 [6.37]	(8.34) ([8.20])	21
90% dark	9.70 ± 0.07	2.410 ± 0.017	0.279 ± 0.007	4.03 ± 0.04	1.103 ± 0.004	4.94 [6.00]	6.15 [7.01]	5.81 [5.98]	17
Dark	10.27 ± 0.04	2.465 ± 0.009	0.247 ± 0.005	4.168 ± 0.023	1.0984 ± 0.0028	5.23 [6.35]	6.29 [7.03]	5.14 [5.25]	8

	$^{4}He_{rad}$	$^{40}Ar_{rad}$	R4[c]	R40[c]
2b-7	78.7 ± 2.5	719 ± 1.7	276 ± 8	1450
2b-14	101.4 ± 2.4	611 ± 1.4	354 ± 8	1300
Light small	65 ± 5	680 ± 410	245	(1400)
Light	53 ± 4	205 ± 8	200	550
Dark small	74 ± 5	1510 ± 960	280	(2310)
90% dark	87 ± 4	726 ± 18	325	1460
Dark	171 ± 5	1074 ± 27	630	1890

[a]For N01-2b-14, ^{36}Ar was not measured. The concentrations of ^{38}Ar and ^{40}Ar are given instead of the $^{36}Ar/^{38}Ar$ and $^{40}Ar/^{36}Ar$ ratios, respectively. The radiogenic ^{4}He is based on a cosmogenic $^{4}He/^{3}He$ ratio of 5.5.

[b]Cosmic-ray exposure age in Ma, calculated with the following production rates derived from Leya and Masarik (2009), in 10^{-8} cm^3 STP g^{-1} Ma: $^{3}He = 1.96$; $^{21}Ne = 0.392$; $^{38}Ar = 0.0481$.

[c]Gas-retention age in Ma, calculated assuming L chondritic abundances of K, U, Th (Wasson and Kallemeyn 1988). The two "small" samples of 2.3 and 2.5 mg, respectively, were measured initially to verify the presence of solar noble gases that could otherwise harm the detectors. The small samples released sufficiently abundant He and Ne, but the Ar, K, and Xe abundances were too small for precise measurements.

All concentrations are given in 10^{-8} cm^3 STP g^{-1}. Typical errors for samples 7 and 14 are approximately 3% for concentrations and approximately 0.5% for ratios. The samples, wrapped in an aluminum foil, were exposed to ultra-high vacuum for several days and preheated at approximately 90 °C. The gases were extracted by pyrolysis in a Mo crucible in a single temperature step at approximately 1800 °C (extraction for 30 min). Complete release of Kr and Xe was checked with a re-extraction step at the same temperature, which contributed 18–23% of the totally released Kr and 8–15% of the Xe. Argon was separated from He and Ne using a charcoal cooled with liquid nitrogen.

Table 9b. Krypton abundances and isotope ratios (^{84}Kr = 100) in Novato samples.

Sample	^{84}Kr	$^{78}Kr/^{84}Kr$	$^{80}Kr/^{84}Kr$	$^{82}Kr/^{84}Kr$	$^{83}Kr/^{84}Kr$	$^{86}Kr/^{84}Kr$
Light small	1.7 ± 0.6[a]	1.1 ± 0.8	5.3 ± 2.0	18 ± 8	23 ± 14	36 ± 18
Light	1.00 ± 0.14[b]	0.68 ± 0.16	4.5 ± 0.8	20 ± 4	20 ± 4	29 ± 5
Dark small	1.4 ± 0.6[a]	n.d.	7 ± 3	20 ± 12	31 ± 22	35 ± 23
Dark	1.56 ± 0.10[c]	0.52 ± 0.10[d]	4.2 ± 0.5	20.3 ± 1.7	20.7 ± 1.9	30 ± 3
90% dark	1.95 ± 0.10[c]	0.53 ± 0.07	4.1 ± 0.4	20.9 ± 1.8	21.2 ± 1.8	31.9 ± 2.6

[a]No Kr detected in re-extraction.
[b]No check for complete degassing by re-extraction, 20 ± 3% added based on ^{84}Kr amount released in re-extraction of the "dark" and "90% dark" samples.
[c]The re-extraction steps of "dark" and "90% dark" released 23% and 18%, respectively, of each total. Isotope abundances of both extraction steps were added—where detected.
[d]Peak ^{78}Kr in re-extraction step not correctly centered and not considered to calculate ratio.
n.d. = not detected, concentrations are given in 10^{-10} cm^3 STP g^{-1}.

Table 9c. Xenon abundances and isotope ratios (^{132}Xe = 100) in Novato samples.

Sample	^{132}Xe	$^{124}Xe/^{132}Xe$	$^{126}Xe/^{132}Xe$	$^{128}Xe/^{132}Xe$	$^{129}Xe/^{132}Xe$	$^{130}Xe/^{132}Xe$	$^{131}Xe/^{132}Xe$	$^{134}Xe/^{132}Xe$	$^{136}Xe/^{132}Xe$
Light small	0.66 ± 0.06	0.5 ± 0.4	n.d.	5.7 ± 1.2	127 ± 14	14.3 ± 1.7	82 ± 13	41 ± 7	33 ± 5
Light	1.00 ± 0.04	0.52 ± 0.03	0.425 ± 0.028	8.1 ± 0.4	112 ± 6	16.1 ± 0.9	81 ± 5	36.5 ± 2.0	31.8 ± 1.8
Dark small	0.99 ± 0.07	n.d.	0.79 ± 0.27	8.1 ± 1.1	119 ± 10	16.1 ± 1.4	88 ± 8	36 ± 5	33 ± 4
Dark	1.252 ± 0.025	0.474 ± 0.028	0.427 ± 0.027	8.2 ± 0.3	108 ± 4	16.4 ± 0.7	80 ± 3	38.0 ± 1.5	31.6 ± 1.3
90% dark	0.959 ± 0.025	0.44 ± 0.03	0.38 ± 0.04	8.0 ± 0.4	114 ± 6	15.5 ± 0.9	82 ± 4	38.7 ± 2.0	31.7 ± 1.7

n.d. = not detected, concentrations are given in 10^{-10} cm^3 STP g^{-1}.

pre-atmospheric mass of 50–120 kg. This size is consistent with the 30–60 cm diameter derived from infrasound and optical measurements of the Novato fireball.

Another indication of pre-atmospheric size is provided by the cosmogenic $^{22}Ne/^{21}Ne$ ratio, which ranges from approximately 1.06 in large objects (radius >50 cm) to approximately 1.25 in small objects (radius <15 cm). The low $^{22}Ne/^{21}Ne$ ratio of approximately 1.09 in Novato suggests moderate shielding. The smallest exposure conditions compatible with the measured value, according to the model of Leya and Masarik (2009), correspond to a shielding depth of 20 cm in an object with a minimum radius of 30 cm.

These shielding conditions are much higher than those derived from the radionuclides, and would correspond to a ^{60}Co activity of approximately 20 dpm kg^{-1}, at least an order of magnitude higher than observed in Novato N01. This apparent discrepancy can be explained by a complex (two-stage) exposure history, in which most of the cosmogenic Ne was produced in a larger object, whereas most of the radionuclides were produced in the last few Ma while Novato was part of a smaller object. This scenario would imply that Novato experienced a collisional break-up event >3 Ma ago, i.e., long enough to reach saturation levels for the radionuclides, including ^{26}Al and ^{10}Be.

Cosmic-Ray Exposure Age

CRE ages of chondrites are generally derived from measured concentrations of cosmogenic ^{3}He, ^{21}Ne, and ^{38}Ar and production rates that are either based on empirical relationships with the $^{22}Ne/^{21}Ne$ ratio (e.g., Eugster 1988), or on purely physical model calculations (Leya and Masarik 2009). Using the ^{3}He, ^{21}Ne, and ^{38}Ar production rates in L chondrites from Eugster (1988) yields CRE ages of 6.2, 6.7, and 5.9 Ma, respectively, while similar ages are obtained using the model of Leya and Masarik (2009). The $^{3}He/^{21}Ne$ versus $^{22}Ne/^{21}Ne$ ratios in Novato are consistent within uncertainty (approximately 5%) with the general trend-line for ordinary chondrites known as the "Bern-plot" (Eberhardt et al. 1966; Nishiizumi et al. 1980). This suggests that Novato suffered relatively little (if any) loss of cosmogenic He. The low $^{3}He/^{21}Ne$ ratio of approximately 3.8 supports the high average shielding conditions that were inferred from the $^{22}Ne/^{21}Ne$ ratio.

The production rates of cosmogenic ^{26}Al and ^{21}Ne in chondrites show similar shielding dependency, so the $^{26}Al/^{21}Ne$ production rate ratio is relatively constant (Graf et al. 1990). The semi-empirical model of Graf et al. (1990) suggests a $^{26}Al/^{21}Ne$ production rate ratio of 0.40 atom/atom for a $^{22}Ne/^{21}Ne$ ratio of 1.09, while the model calculations of Leya and Masarik (2009) suggest

Table 10. Thermoluminescence data for the light and dark lithologies of the Novato meteorite N01-1e[a]. Natural thermoluminescence (NTL) and thermoluminescence sensitivity (TL) normalized to Dhajala are given. T_p is the profile peak temperature, while W_p is the profile full width at half maximum.

	NTL (krad)	TL sens (Dhajala = 1)	T_p (°C)	W_p (°C)
Novato dark	6.6 ± 1.8	0.028 ± 0.007	180 ± 20	155 ± 15
Novato light	12.8 ± 2.8	0.029 ± 0.007	187 ± 14	153 ± 18

[a]Uncertainties are 1σ based on triplicates.

that the production ratio varies from 0.35 in large objects to 0.41 in small objects. Adopting an average $^{26}Al/^{21}Ne$ production rate ratio of 0.38 ± 0.03 atom/atom, we calculate a shielding-independent CRE age of 9 ± 1 Ma for Novato. A similar age of approximately 9 Ma is derived from the $^{10}Be/^{21}Ne$ ratio using the production ratio of 0.14 ± 0.01 atom/atom (Graf et al. 1990).

This 9 Ma exposure age overlaps with a well-defined peak at approximately 10 Ma in the CRE age histogram of L chondrites having low radiogenic ^{40}Ar contents (Marti and Graf 1992). There is still some uncertainty regarding the CRE age, as part of the cosmogenic Ne may have been produced in a first-stage exposure under high shielding conditions. Based on the current data set, we cannot constrain the first-stage exposure conditions of Novato, but it seems likely that the change in shielding conditions occurred during a collision in the last 3–5 Ma.

Thermal Resetting Events

Both He and Ar contain radiogenic ^4He and ^{40}Ar. Past heating events are documented by K-Ar as well as U,Th-He ages. In samples N01-2b-7 and N01-2b-14, also analyzed for cosmic-ray exposure ages, the measured radiogenic ^4He and ^{40}Ar (Table 9) can be used to determine a K-Ar and U,Th-He age, assuming L chondritic concentrations of K (825 ppm), U (13 ppm), and Th (43 ppm) (Wasson and Kallemeyn 1988). The elemental concentrations of Th, U, and K in Novato N01 measured at LNGS are listed in Table 8b. They agree well with the average concentrations given in Wasson and Kallemeyn (1988).

The U,Th-He age is between 200 and 630 Ma. The K-Ar ages of the samples are between 550 and 1890 Ma. Some of these variations may be due to the small sample size, in which the K content may not have been homogeneously distributed. However, all shocked L chondrites examined by Korochantseva et al. (2007) were prone to partial Ar loss during the 470 Ma shock event, resulting in higher K-Ar ages. If Novato lost its radiogenic Ar in the same way, Ar was also not completely degassed during that event.

Novato does not contain solar wind He and Ne, nor is the He/Xe ratio solar (Table 9). The absence of any solar wind component shows that Novato is not a regolith breccia originating from the outermost layers of its parent body, but rather a fragmental breccia. Whereas regolith breccias are relatively rare among L chondrites (approximately 3%; Bischoff and Schultz 2004), fragmental breccias are not (22%; Rubin et al. 1983).

The initial samples, having masses of 2.3 and 2.5 mg, were too small to get precise values for trapped gas components. Larger samples, weighing 16–18 mg, allowed better determinations. The trapped Kr and Xe isotopic composition is consistent with both phase Q (Busemann et al. 2000) and air composition. The $^{84}Kr/^{132}Xe$ ratios of all samples (approximately 1–2) suggest that the trapped gas is Q-gas. The light/dark/90%-dark fragments show similar Ar–Xe abundances and isotope ratios including similar excesses in ^{129}Xe ($^{129}Xe/^{132}Xe$~1.1–1.3). None of the samples shows excess in $^{80,82}Kr$ and –Xe from an enhanced neutron fluence, converting Br and I into noble gases, suggesting again an origin of the Novato sample from deeper layers below the surface of the parent body, or low halogen abundances.

Anomalous Kr and Xe due to fission were not detected. Cosmogenic ^{83}Kr and ^{126}Xe could not be determined due to the small sample size, low target element concentrations, and the relatively short exposure age. The low trapped Kr and Xe concentrations are within the expected range for severely metamorphosed nonregolithic (gas-poor) ordinary chondrites. All samples show an excess of ^{129}I-derived ^{129}Xe, suggesting that the Xe-containing minerals in Novato were closed for Xe-loss while ^{129}I ($t_{1/2}$~15.7 Ma) was still alive and not inhomogeneously reset anytime after closure.

More Recent Heating Events

Novato experienced a relatively recent (<10^5 yr) heating event (which did not erase the ^{129}I-derived $^{129}Xe/^{132}Xe$ signature), according to thermoluminescence (TL) measurements at NASA Ames Research Center. A chip of dark lithology and a chip of light lithology were taken well clear of the fusion crust, and their TL properties (Sears et al. 2013) were measured for duplicate aliquots of each chip. The natural TL level of both light and dark lithologies was very low (Table 10),

6.6 ± 1.8 krad for the dark lithology and 12.8 ± 2.4 krad for the light lithology, compared to 50–100 krad more typical of fresh ordinary chondrites falls (Benoit and Sears 1994). The low level implies a reheating event (to about 200–300 °C) within the last approximately 10^5 yr, this being the time it typically takes for natural TL to reach equilibrium (Benoit and Sears 1994). The cause of the heating is unclear. A small perihelion or atmospheric heating are clearly not the explanation, which leaves a recent shock event in space as most likely.

The TL sensitivity of the dark and light lithology was identical: 0.028 ± 0.007 and 0.029 ± 0.007, respectively, normalized to Dhajala meteorite = 1. These values are typical of low petrographic type 3.2 (Sears et al. 1980), but this is precluded by the mineralogy and petrology and by the temperature and width data of the induced TL peak, which are consistent with those of equilibrated ordinary chondrites (Table 10). The TL sensitivity data suggest that the samples examined here are more heavily shocked than the sample examined petrographically and, perhaps surprisingly, that the light lithologies are as heavily shocked as the dark lithologies. The low TL sensitivity suggests a high shock level of S5–S6 on the scale devised by Stöffler et al. (1991), with shock levels in excess of 40 GPa (Hartmetz et al. 1986).

Collisional Compaction

Novato experienced a strong compaction and the most recent impact event recorded in the orientation of metal grains was quite intense. The orientation and intensity of shock-induced foliation of metal grains were derived from X-ray microtomography data collected at UC Davis (Fig. 3), using methods found in Friedrich et al. (2008, 2013). The metal grains within the tomographic volumes were digitally isolated and best-fit ellipsoids were drawn around each. The orientation of the foliation is shown in Fig. 17 as the direction of the long axis of each ellipsoid.

To obtain a quantitative value for the intensity of foliation, we used a variation of the orientation tensor method: the natural logarithm of the ratio of major over minor eigenvalues of the ellipsoids is computed to yield a strength factor (Woodcock 1977; Woodcock and Naylor 1983). The higher the strength factor, the greater the common orientation of the metal grains in the sample and the greater the compaction/shock loading apparent in the material volume under investigation.

The Novato N05 and N06 stones have extremely well-developed petrofabric, with a stronger strength factor than those seen for most other ordinary chondrites of shock-stage S4–S6 (Fig. 18). The shock-induced petrofabrics in Novato N05 and N06 are similar in both intensity and orientation, indicating each experienced an identical (most recent) impact history.

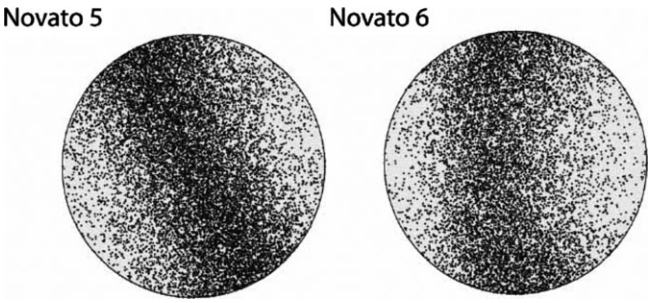

Fig. 17. Stereoplot of major axis orientations of all individual metal grains in two different stones of the Novato L chondrite. The orientations of the stones in the meteoroid relative to one another are unknown. However, the intensity of foliation is nearly identical between the two fragments, suggesting that both experienced the same impact event.

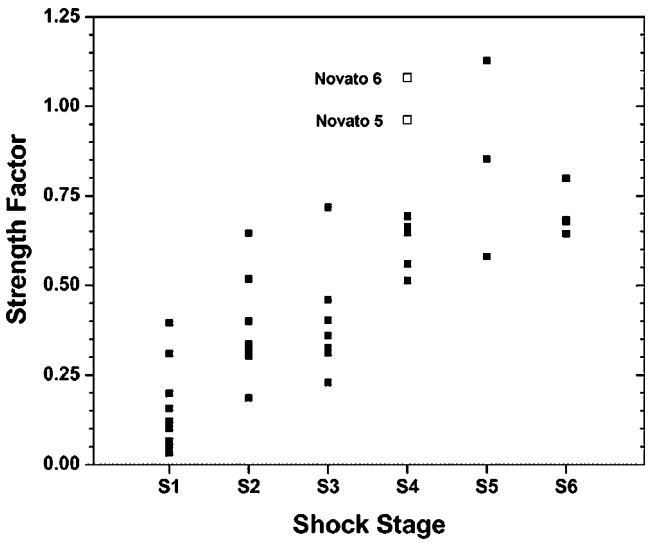

Fig. 18. Degree of compaction, given by the strength factor determined from the collective orientation of metal grains in ordinary chondrites versus shock-stage (Friedrich et al. 2008, 2013). Novato shows significant foliation in both samples examined.

ORGANIC MATTER

Organic compounds illuminate the chemistry induced by thermal alteration of the rock, and depend on the mineral chemical composition, morphology, distribution of impurities, and the presence of structural and/or electronic defects (Schoonen et al. 2004; Kleber et al. 2007; Le Guillou et al. 2012). Shocked ordinary

chondrites are not expected to contain high levels of organic compounds, but experimental techniques today are sufficiently sensitive to detect trace amounts (Schmitt-Kopplin et al. 2012). Novato N01 was recovered before exposure to rain. Since it has a low porosity, contamination by the terrestrial environment and from handling may not have penetrated deeply into the stone.

In the next sections, we report on the detection of several types of organic compounds, namely methanol soluble compounds, amino acids, insoluble polyaromatic hydrocarbons (PAHs), and higher molecular weight macromolecular carbon, respectively. Amino acids are among the smallest and most easily contaminated compounds. Because terrestrial contaminants from the environment and from handling are mostly L-type amino acids, measurements of the relative abundances of D- to the L- enantiomers (the D/L ratio) can be used to infer the level of protein amino acid contamination. We find that some contamination has occurred, but at a low enough level to still be able to detect the intrinsic amino acids, especially nonprotein amino acids that are rare on Earth. That means that many other heavier compounds presented here are likely intrinsic as well, confirmed by the presence of consistent homologous structural series in mass spectrometry.

Methanol Soluble Organics

The organic analysis of methanol soluble organic compounds was performed on a 3.6 g freshly broken off fragment of Novato N01 at the Helmoltz Zentrum in Munich (N01-2, Fig. 1), immediately after gamma-ray counting of the whole rock was completed in late December. From the freshly fractured face, around 200 mg (N01-2a) was collected from both the light chondritic and the shock-darkened zones for destructive methanol solvent extraction of organics and analysis with ion cyclotron resonance Fourier transform mass spectrometry (ICRFT/MS), as well as with nuclear magnetic resonance spectroscopy (NMR) as described in Schmitt-Kopplin et al. (2010, 2012) and Popova et al. (2013). The method extracts preferentially the polar/protic molecules into methanol and results do not pertain to insoluble compounds such as PAHs.

Results from ultrahigh resolution mass spectrometry (resolution of 500,000 at m/z 400 with a mass precision of 0.1 ppm) show the typical aliphatic signatures in composition, with homologous series of hundreds of compounds (Fig. 19). The presence of homologous series implies that this is intrinsic soluble organic matter. Contaminants weigh in general lower than 1% of the signal amount and generally break the rule of continuous structural features with very intense signals; these are generally fatty acids and anthropogeneous alkylsulfonates.

The nontargeted organic structural spectroscopy (Hertkorn et al. 2007) identified thousands of ionizable polar compounds in the mass range from 140 to 2000 amu. Aliphatic molecules were more abundant than aromatic molecules. However, the dark material contained relatively larger proportions of aromatic compounds (H/C lower than 1) than the light material. All fractions showed the highest intensity for CHO molecules, but CHOS and CHNO compounds also show strong signals (0.1 amu mass detail in Fig. 19). The dark material seems to comprise less CHOS compounds than the light material, but larger proportions of more nitrogen-containing compounds, some of which have several nitrogen atoms, corresponding to the recent observations of the LL5 Chelyabinsk chondritic and shock-darkened materials (Popova et al. 2013).

Nuclear magnetic resonance (^{1}H NMR) spectra of the methanolic extracts (Fig. 20) provide further structural constraints and insight into the chemical environments of the organic compounds (Quirico et al. 2003). NMR section integrals are presented in Table 11. The ^{1}H NMR spectra show a considerable diversity of purely aliphatic branched and some alicyclic compounds (CCC**H** units, in bold the atom whose nearby environment determines the NMR signal), with the presence of approximately 7% of cyclic and open chain carboxylic acids (according to the α-proton NMR integral, Table 11).

^{1}H NMR spectra of the dark and light lithologies indicated different ratios of key aliphatic branching motif units rather than a manifest chemical diversity of functional groups: the dark lithology extract showed higher proportions of methyl in branched, perhaps alicyclic molecules (i.e., on average smaller molecules than found in the chondritic extract) and carboxylic acids. The percentage ratio of CC**H**/OC**H**/C_{sp2}**H** units was found near 85/10/5, suggesting a higher abundance of pure compared with functionalized aliphatic environments. The olefin/aromatic NMR integral ratio was nearly equal; doubly fused and higher aromatics (δ_H >7.3 ppm) dominated the aromatic ^{1}H NMR signature. ^{1}H NMR signatures of aliphatic OCH units differed for dark and light lithology extracts; however, the ether/hydroxyl (δ_H <4 ppm) to ester (δ_H >4 ppm) ratio ranged near 5:1 for both extracts.

Pronounced aliphatic branching (Remusat et al. 2005) was indicated by the larger proportions of methyl C-(C_2)CH-C**H$_3$** adjacent to methylene groups than C-CH_2-C**H$_3$** (ethyl) groups in J-resolved NMR spectra (data not shown). Similarly, $^3J_{HH}$ double-doublet splittings of ether/hydroxyl with $\delta_H \approx 3.4$–

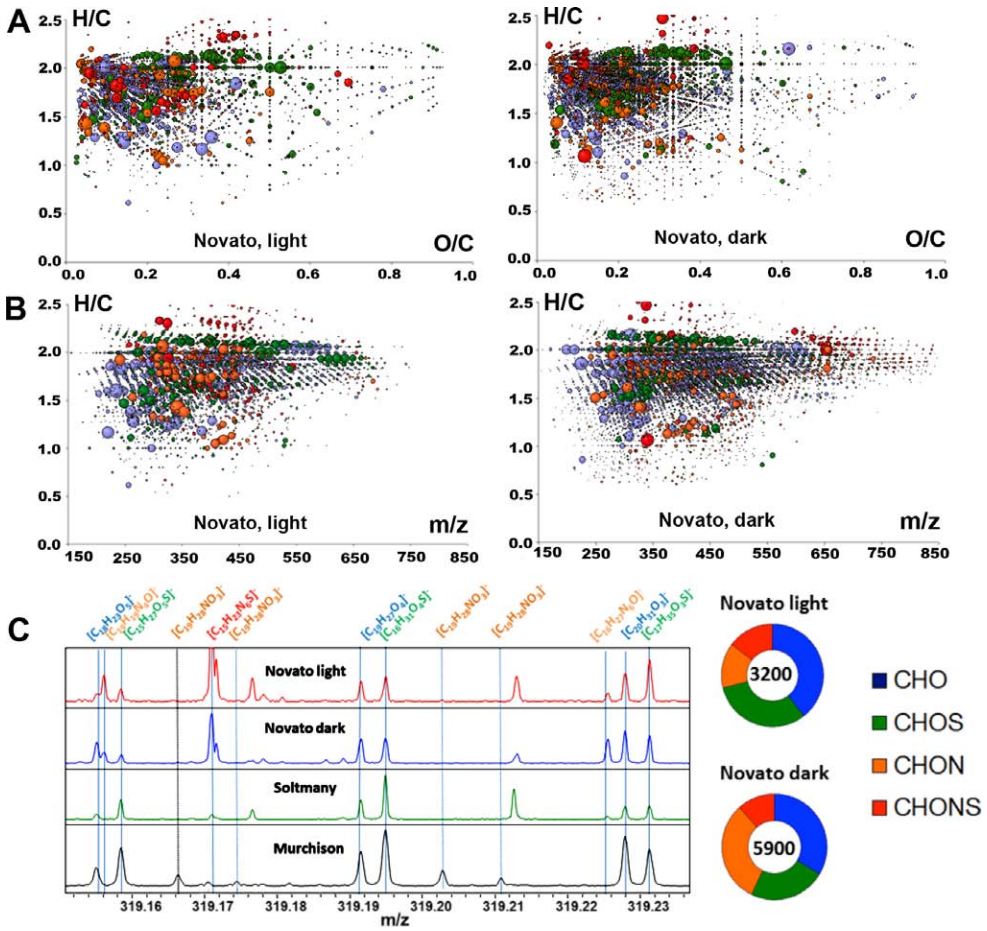

Fig. 19. Ion cyclotron resonance Fourier transform mass spectrometry (ICRFT/MS). Visualization of the compositional space of Novato light lithology (3200 assigned compositions) and dark lithology (5900 assigned compositions) fractions as analyzed with ESI(-)-ICR/FTMS. The van Krevelen diagrams (A) show rather aliphatic type of structures with a prevalence of CHO and CHOS type molecules in the chondritic phase and an increase in the count of CHNO compounds in the impact melt. The lower diagrams show the H/C changes by molecular mass (B) and the presence of regular homologous series up to higher masses. The area of each circle is proportional to the intensity of the detected mass peak. Colors mark compounds containing only CHO (blue), CHOS (green), CHNO (orange), or all CHNOS (red) molecules. The 0.1 amu mass spectra details from mass 319.15 to 319.25 (C) show the importance of the nitrogen compounds in the dark fraction and compare its specific organic signature and its complexity with Soltmany and Murchison meteorite extracts.

3.7 ppm and ester groups ($\delta_H \approx 4.2$ ppm) suggested the presence of CH-(O)C**H**-CH– units in possibly cyclic arrangements. Two sets of olefins ($\delta_H \approx 5.32$ and 5.34 ppm; 3% of ^{1}H NMR integral) with opposite abundance ratios in light and dark lithology extracts were present. Here, the high frequency set showed total correlation apectroscopy cross peaks to aliphatic positions ($\delta_H \approx 2.05$ and 1.43 ppm), suggesting incorporation of a double bond in an aliphatic chain. A few cross peaks in ^{1}H, ^{13}C heteronuclear single quantum coherence NMR spectra indicated branched aliphatics also at $\delta_H \approx 1.28$ ppm (polymethylene and branched aliphatics, with $\delta_C \approx 22$–33 ppm) and the presence of certain oxomethylene (OCH_2) groups with $\delta_C \approx 60$–76 ppm (Table 11).

Amino Acids

The remains of the two Novato methanol extracts from approximately 50 mg samples of the N01 light and dark lithologies were subsequently analyzed at NASA Goddard Space Flight Center for amino acids as an indicator of terrestrial contamination of the meteorite samples in the period shortly after the fall. This targeted analysis of amino acids pertains to smaller molecules than analyzed above. Freshly fallen L chondrites typically have very low levels of soluble organics.

The methanol extracts were dried under vacuum, acid hydrolyzed under 6M HCl vapor at 150 °C for 3 h, desalted by cation exchange chromatography, and derivatized with *o*-phthaldialdehyde/*N*-acetyl-L-cysteine

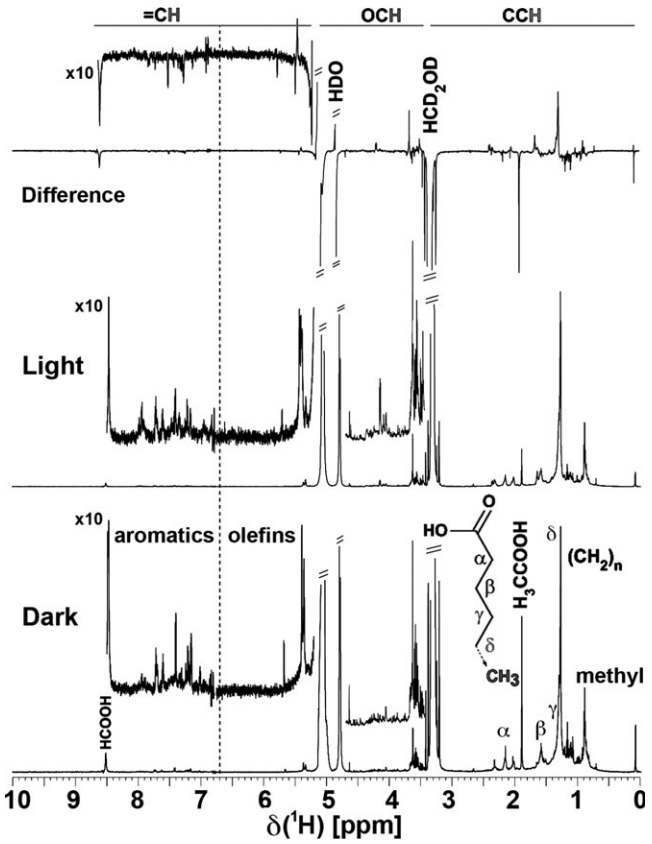

Fig. 20. One-dimensional ^{1}H NMR spectra (800 MHz, CD_3OD) of shock-darkened material (Dark), light chondritic material (Light), and the difference of these NMR spectra (Difference), shown with insert of unsaturated protons with increased amplitude (×10). The main substructures are indicated. The NMR resonance at chemical shift $\delta_H = 1.25$ ppm is primarily composed of superimposed NMR peaks resulting from various branched aliphatics. HCOOH and CH_3COOH are common byproducts of SPE-DOM (solid phase extraction—desolved organic matter), possibly resulting from degradative reactions.

Table 11. Summary of ^{1}H NMR section integrals for light and dark lithology methanolic extracts.

$\delta(^{1}H)$ [ppm]	Novato light	Novato dark
10.0–5.0	4.4	6.1
5.0–3.1	11.5	9.9
3.1–1.9	10.3	9.8
1.9–1.35	16.1	19.7
1.35–1.25	31.9	25.8
1.25–1.0	10.6	13.8
1.0–0.5	15.2	15.0
Sum	100.0	100.0

(OPA/NAC) and then analyzed for amino acids with chiral separation using a liquid chromatography with fluorescence detection and time-of-flight mass spectrometry (LC-FD/ToF-MS) as previously described (Glavin et al. 2006, 2010). Although the different extraction technique may affect the outcome, the Novato extracts had about 1000 times less of the nonprotein α-aminoisobutyric acid abundance than that found in CM2 Murchison, and about the same low value found for a freshly collected H6 chondrite sample of Almahata Sitta (Burton et al. 2011).

Results show that the amino acid distributions and enantiomeric ratios (D/L) in methanol extracts from the light and dark lithologies were similar (Table 12). Several common terrestrial protein amino acids including glycine, serine, aspartic and glutamic acids, alanine, and valine were detected with relatively low D/L ratios ranging from approximately 0.06 to 0.25, suggesting that some terrestrial L-amino acid contamination of the samples has occurred. However, we cannot rule out the possibility that trace levels (approximately 2–8 ppb) of the nonprotein amino acids α-aminoisobutyric acid, DL-α-amino-*n*-butyric acid, and racemic DL-β-amino-*n*-butyric acid (Table 12), which are typically very rare on Earth, are indigenous to the Novato meteorite. Compound-specific stable isotope measurements are needed to firmly establish the origin of these nonprotein amino acids in Novato.

Polyaromatic Hydrocarbons

The meteorite also contains nonsoluble organic compounds in the form of polyaromatic hydrocarbons (PAHs). A freshly broken fragment of Novato N01-1b (dark lithology) was analyzed by laser desorption laser ionization mass spectrometry (L^2MS) (Wu et al. 2013) at Stanford University, a technique that involves no solvent. A rich mass spectrum of compounds was detected, as shown in Fig. 21. The mass spectrum shows an abundance of atoms and molecules having a low ionization potential. The peak at $m/z = 26$ indicates the existence of CN groups. Molecular weights of odd number are dominant, which suggests the presence of N atoms in the compounds. The signal at $m/z = 91$ is believed to be $C_7H_7^+$, which is commonly observed in PAHs. These results suggest that most of the low-ionization-energy compounds in Novato N01 are PAHs with either N atoms in the ring or in side chains. For example, the possible formula of molecules at $m/z = 107$ is C_7H_9N, which might be toluidine or *N*-methylaniline among other possibilities. Some elements are clearly observed also, such as Na^+ at $m/z = 23$, Mg^+ at 24, and K^+ at $m/z = 39$ and 41. The peaks at $m/z = 206$, 207, and 208 might arise from Pb as the intensity distribution fits well the expected isotope abundances of this element. Higher mass peaks than this are not observed.

Table 12. Summary of the amino acid analysis of the light and dark lithologies from methanol spray sampling of Novato N01-2a.[a]

Amino acid	Novato light (ppb)	D/L ratio	Novato dark (ppb)	D/L ratio
D-Aspartic acid	53 ± 2	0.19 ± 0.01	23 ± 4	0.25 ± 0.05
L-Aspartic acid	281 ± 1		90 ± 8	
D-Glutamic acid	83 ± 5	0.11 ± 0.01	47 ± 9	0.15 ± 0.03
L-Glutamic acid	768 ± 54		316 ± 5	
D-Serine	<4	<0.01	<2	<0.01
L-Serine	444 ± 13		199 ± 54	
Glycine	398 ± 152	–	111 ± 17	–
β-Alanine	<3	–	<3	–
γ-Amino-*n*-butyric acid	9 ± 2	–	7 ± 1	–
D-Alanine	18 ± 2	0.15 ± 0.09	9 ± 1	0.12 ± 0.04
L-Alanine	120 ± 71		76 ± 25	
D-β-Amino-*n*-butyric acid	3 ± 2[b]	~1	2 ± 1[b]	~1
L-β-Amino-*n*-butyric acid	3 ± 2[b]		2 ± 1[b]	
α-Aminoisobutryic acid	6 ± 2[b]	–	7 ± 3[b]	–
DL-α-Amino-*n*-butyric acid[c]	6 ± 5[b]	nd	8 ± 5[b]	nd
DL-Isovaline	<5	nd	<5	nd
ε-Amino-*n*-caproic acid	8 ± 6	–	15 ± 2	–
D-Valine	9 ± 3	0.06 ± 0.02	<6	<0.19
L-Valine	144 ± 2		32 ± 7	

[a]Novato N01-2a meteorite methanol extracts (light and dark lithologies) were analyzed by OPA/NAC derivatization (15 min) and LC separation with UV fluorescence (LC-FD) and time of flight mass spectrometry (TOF-MS) detection. For the LC-FD/TOF-MS data, the fluorescence peaks and the mono-isotopic masses of each protonated OPA/NAC amino acid derivative ($M + H^+$) were used for quantification and final peak integrations included background level correction using a procedural blank and a comparison of the peak areas with those of an amino acid standard run on the same day. The final values were normalized using the desalting and derivatization recoveries of an internal D,L-norleucine standard (recoveries ranged from 60 to 70% for the meteorite extracts). The uncertainties (δx) are based on the standard deviation of the average value of three separate measurements (n) with a standard error, $\delta x = \sigma_x ((n-1)^{-1/2}$.

[b]Tentatively detected above blank levels.

[c]Enantiomers could not be separated under the chromatographic conditions.

Macromolecular Carbon and Carbon and Nitrogen Isotopes

To study the total carbon and nitrogen content and isotopic compositions, two fragments (one light, one dark) from Novato N01-1e (Fig. 1) were analyzed by stepped combustion–gas source mass spectrometry (SC-GC-MS) at the Open University, U.K. Results from the analyses are given in Table 13 and Fig. 22. The dark fractions of Novato contained 611.3 ppm carbon with weighted $\delta^{13}C \sim -39‰$. Carbon abundance in the light fraction was much lower, at 97.6 ppm with weighted $\delta^{13}C \sim -27‰$. Unfortunately, in both analyses, so much SO_2 was released at temperatures above 500 °C (light fraction) and 700 °C (dark fraction) that CO_2 isotope measurements were compromised, and could not be determined.

The carbon released from both fractions was mainly below 600 °C, although in the dark fraction of N01-1e, there was a second maximum between 900 and 1000 °C (Fig. 22). The maximum combustion temperature of 600 °C implies that most of the carbon occurs as an organic macromolecular component, or poorly graphitized carbon. Nitrogen was not affected by sulfur dioxide, and so both abundance and isotopic data were collected throughout the whole experiment. Again, there

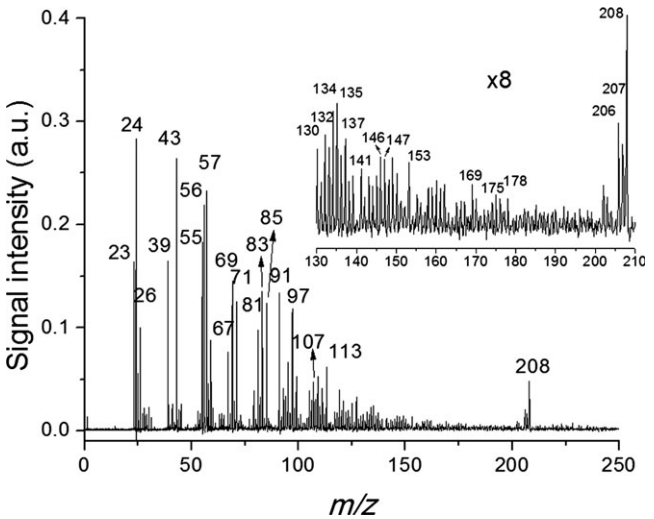

Fig. 21. L^2MS spectrum of Novato N01-1b. Inset shows an enlarged portion of the mass spectrum.

Table 13. Carbon and nitrogen stepped combustion data from Novato N01-1e.

Temp. (°C)		Total (<1400)			200–400			400–600		
	Wt (mg)	[C] (ppm)	$\delta^{13}C$ (‰)	C/N (at)	[C] (ppm)	$\delta^{13}C$ (‰)	C/N (at)	[C] (ppm)	$\delta^{13}C$ (‰)	C/N (at)
Dark	4.788	611.3	−39	–	76.9	−24	11–22	439.5	−43	53–215
Light	6.089	97.6	−27	–	33.8	−26	58	14.9	−25	28
		[N](ppm)	$\delta^{15}N$(‰)		[N](ppm)	$\delta^{15}N$(‰)		[N](ppm)	$\delta^{15}N$ (‰)	
Dark	4.788	13.9	+4.8		6.0	+1.9		4.8	+2.0	
Light	6.089	3.0	−2.1		0.7	−4.4		0.6	−2.6	

Experimental procedures were as follows: Uncrushed chips of material were weighed into platinum foil, then loaded into the Finesse SC-GC-MS system. The samples were heated under pure oxygen for approximately 40 min at each temperature; the resulting combustion products were then cryogenically separated for analysis into carbon dioxide and nitrogen. Sulfur dioxide and water were also produced and separated, but not analyzed. The temperature program for the experiments was of increments of 100 °C from room temperature to 1400 °C. CO_2 and N_2 were analyzed on separate triple collector gas-source mass spectrometers. Errors on the analyses were ±1‰ for CO_2, with the minimum amount of gas measured approximately 1 ng. For nitrogen, the error on the analysis was ±0.5‰, and minimum sample size was approximately 0.5 ng.

was a difference in the results for the two fractions, the dark having 13.9 ppm with $d^{15}N$ of ~+4.8‰, whilst there were only 3.0 ppm nitrogen in the light fraction with $d^{15}N$~−2.1‰. In each sample, almost all the nitrogen was liberated by 600 °C, implying its association with a carbonaceous host.

Looking at the individual profiles of Novato 01 (Fig. 22), and focusing only on the material which was released below 600 °C, it is clear that there are at least two components in the dark fraction that combust in this temperature increment. Up to 400 °C, 76.9 ppm carbon with $\delta^{13}C$~−24‰ is liberated. There is then a steep drop in isotopic composition, down to $\delta^{13}C$~−43‰ for almost 440 ppm carbon. In contrast, although there are two separate maxima in nitrogen yield (at 200–400 °C and 400–600 °C), the isotopic composition of the nitrogen ($\delta^{15}N$~+2‰) is almost constant across the temperature interval.

The lower temperature material (with atomic C/N ratio between 11 and 22) is likely to be terrestrial contamination. At least some of the nitrogen will be from adsorbed terrestrial atmosphere. The isotopically light material has an atomic C/N ratio that extends to over 200, which is much higher than the estimated C/N ratio of macromolecular material in chondritic meteorites (approximately 50; Zinner 1988). Values of such a magnitude are consistent with identification of the component as amorphous carbon, or even microcrystalline diamonds (Russell et al. 1991).

The light fraction of Novato 01 had a carbon combustion profile that was much more akin to the results from other equilibrated ordinary chondrites (Grady et al. 1989). Again, the lowest temperature material (this time with C/N of approximately 58) is possibly a terrestrial contaminant; the higher C/N ratio and lower $\delta^{15}N$ (about −4.4‰), implying that less atmosphere is adsorbed than in the dark fraction. C/N ratios of 10–60 are associated with land plants (Dai et al. 2005; Marchand et al. 2005). The second component identified in the dark fraction, with light carbon isotopic composition, seems to be absent from the light fraction.

Equilibrated ordinary chondrites contain very little indigenous carbon (Grady et al. 1989) or nitrogen (Hashizume and Sugiura 1995); any carbon present tends to be either poorly crystallized to crystalline graphite or is dissolved in metal. Nitrogen is assumed to be carried by these phases. The carbon and nitrogen data for the light lithology of Novato 01 fits into this picture. In contrast, the dark lithology displays characteristics that have more in common with unequilibrated ordinary chondrites: a higher abundance of carbon with a combustion temperature and C/N ratio that is consistent with identification of the component as amorphous to poorly crystalline carbon, possibly even microcrystalline diamond. It is unlikely that this material is produced by conversion of indigenous carbon during the shock-blackening process, mainly because its abundance is more than an order of magnitude higher than that in the light fraction, which is taken to represent mean equilibrium ordinary chondrite carbon.

Overall, organic matter studies show an intrinsic organic molecular complexity that mostly originates from chemistry in the meteoroid parent body. Further studies of organic molecular diversity within chondrites will help constrain the conditions of abiotic organic matter formation and evolution.

DISCUSSION

Possible Source Region in the Asteroid Main Belt

Besides Novato, there are four other L chondrite falls with known orbital elements (Table 14a). From Jesenice (Spurny et al. 2010) to Innisfree (Halliday et al.

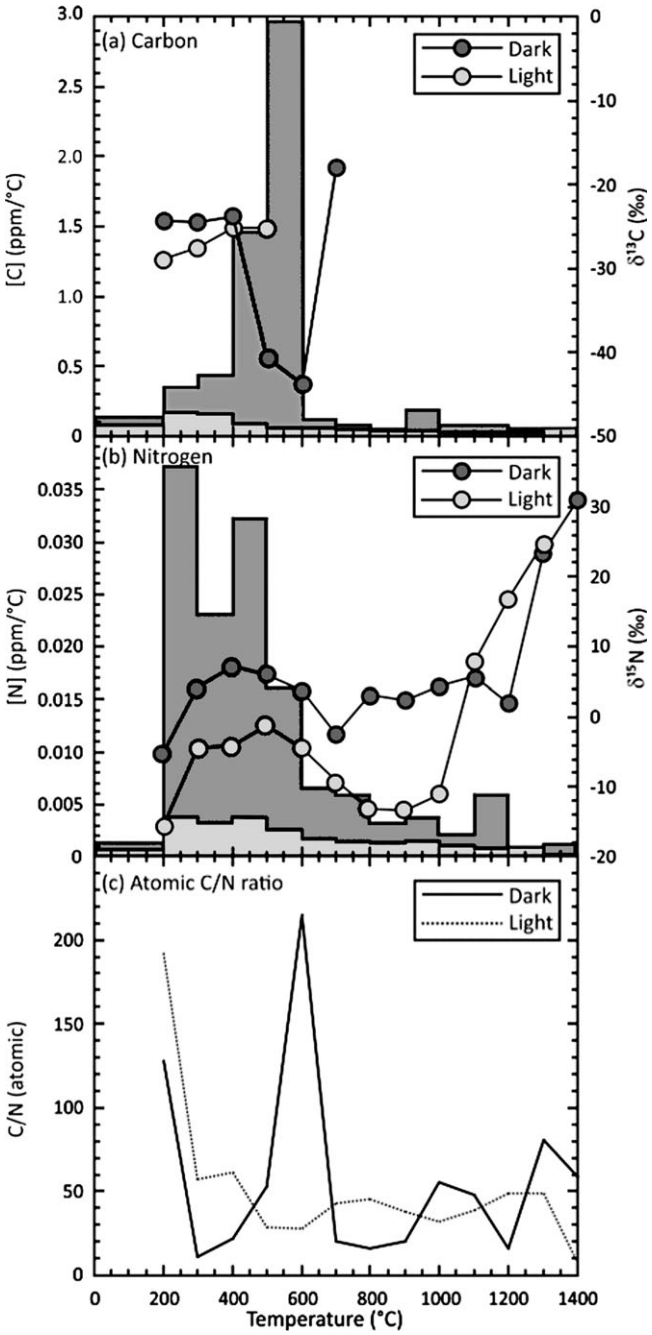

Fig. 22. Data from stepped combustion-gas source-mass spectrometry of light and dark lithologies from Novato 01-1e. (A) carbon, (B) nitrogen, and (C) the atomic C/N ratio. Abundances of carbon and nitrogen are plotted as histograms and scaled on the left-hand axis. Isotopic compositions are plotted as lines and scaled on the right-hand axis. Errors in $\delta^{13}C$ and $\delta^{15}N$ are less than the size of the symbols.

1978, 1981), to Novato (this work), to Villalbeto de la Peña (Trigo-Rodriguez et al. 2006), to Park Forest (Brown et al. 2004), they form a sequence of increasing semimajor axis (a), aphelion distance (Q) and eccentricity (e), and decreasing perihelion distance (q). All have their aphelion in the asteroid belt (Q = 2.5 – 4.3 AU).

A large fraction (possibly all) shocked L chondrites were part of a approximately 100 km-sized parent body that experienced a collision event that re-set the K-Ar age by releasing Ar from the minerals 470 ± 6 Ma (Korochantseva et al. 2007; Weirich et al. 2012a, 2012b). At about the same time, Earth experienced an increase in meteorite influx as indicated by fossil meteorites in Middle Ordovician deposits in Sweden dated to 467.3 ± 1.6 Ma (Schmitz et al. 2001).

Based on its dynamical age, Nesvorný et al. (2009) identified the Gefion asteroid family, located on the inside of the 5:2 mean-motion resonance, as the likely debris field from this collision. The nearby 5:2 resonance offered the initial low-efficiency but quick pathway to Earth in the Ordovician. The efficiency of this resonance is low because before the orbital eccentricity can be increased high enough to have Earth-intersecting orbits, the aphelion of the orbit evolves to cross Jupiter's orbit, as a result of which most meteoroids are deflected from hitting Earth.

A more efficient route is the 3:1 resonance, which has been proposed as the route through which small L chondrite fragments of an ongoing collisional cascade find a path to Earth today. On their way toward evolving to the 3:1 resonance, the meteoroids can remain exposed to cosmic rays for a relatively long time. This was proposed to be the reason why this group does not show a sharp peak in the CRE age distribution (Nesvorný et al. 2009).

Based on the strongly shocked nature of Novato and the 420 ± 220 Ma U,Th-He age, Novato appears to belong to this group of shocked L chondrites. Recently, after completion of the consortium study, Yin et al. (2014) measured the U-Pb ages of apatite grains in Novato and concluded that the final resetting of the U-Pb system was 473 ± 38 Ma ago, in agreement with this statement. The 550–1890 Ma K-Ar age is higher, perhaps only because of Ar loss during the approximately 470 Ma event, which also affected other shocked L chondrites (Korochantseva et al. 2007).

Does Novato's orbit still carry a signature of its source region? That depends in part on how frequently it is catastrophically fragmented. Only if the dynamical evolution is faster than the collisional lifetime, or the breakup is gentle, will the semimajor axis and inclination remain relatively unchanged. The collisional lifetime for near-Earth asteroids from collisions with Main Belt asteroids is about 1.4 $r^{1/2}$ Ma, with r the radius in cm (Wetherhill 1985; Bottke et al. 1993; Farinella et al. 1998; Morbidelli and Gladman 1998). From this, the collisional lifetime for Novato is about 5.9 Ma. This value is similar to the measured CRE age

Table 14a. Overview of other known L chondrite falls with atmospheric trajectory and orbit determinations from photographic and video data (Equinox J2000).

	Jesenice L6	Innisfree L5	Novato L6	Villalbeto de la Peña L6	Park Forest L5
Date	2009-04-09	1977-02-06	2012-10-18	2004-01-04	2003-03-27
Solar longitude (°)	19.196	317.507	204.967	283.671	6.116
Peak brightness (visual magn. @ 100 km)	−15.0 ± 0.5	−12.1	−13.8 ± 1.0	−18	−21.7
Entry speed V_∞ (km s^{-1})	13.78 ± 0.25	14.54	13.67 ± 0.12	16.9	19.5 ± 0.3
Entry angle (°)	59	67.8	19.4 ± 0.1	29.0	61.0
Initial mass (kg)	170 ± 80	20	80 ± 35	760 ± 150	11,000 ± 3000
Initial diameter (cm)	45	20	35 ± 5	70	180
Kinetic energy E_{kin} (kt)	0.004	0.0005	0.003	0.02	0.5
Altitude start (km)	88	>62.4	95	>47	82
Altitude peak brightness (km)	26	36	37	28	29
Altitude end (km)	~18	19.9	21.9[a]	22.2	<18
Final speed (km s^{-1})	–	2.7–4.7	3.1[a]	7.8	–
Mass recovered (kg)	3.6	4.6	0.4	4.6	>18
Orbit-*a* (AU)	1.75 ± 0.07	1.872 ± 0.05	2.09 ± 0.08	2.3 ± 0.2	2.53 ± 0.19
Orbit-*q* (AU)	0.9965 ± 0.0006	0.9862 ± 0.0003	0.9880 ± 0.0001	0.860 ± 0.007	0.811 ± 0.008
Orbit-*e*	0.431 ± 0.022	0.4732 ± 0.015	0.526 ± 0.017	0.63 ± 0.04	0.680 ± 0.023
Orbit-*i* (°)	9.6 ± 0.5	12.28 ± 0.3	5.51 ± 0.04	0.0 ± 0.2	3.2 ± 0.3
Orbit-ω (°)	190.5 ± 0.5	177.97 ± 0.4	347.35 ± 0.13	132.3 ± 1.5	237.5 ± 1.6
Orbit-Ω (°)	19.196 ± 0.001	317.507 ± 0.001	24.9900 ± 0.0035	283.671 ± 0.001	6.1156 ± 0.0007
U,Th-He age (Ma)	1700–2700	–	460 ± 220	–	–
K-Ar age (Ma)	3020–3530	4100 ± 300	550–1890	700	–
Reference	[1]	[2]	[3]	[4]	[5]

[1] = Ott et al. (2010); Spurny et al. (2010); Bischoff et al. (2011); [2] = Beech (2001) (uncertainty calculated by assuming speed uncertain by 0.1 km s^{-1}); Halliday et al. (1978, 1981); Heusser et al. (1978); [3] = Llorca et al. (2005); This work, orbit 2 months prior to impact; [4] = Trigo-Rodriguez et al. (2006); [5] = Brown et al. (2004); Simon et al. (2004).

[a]Derived from photographed final stage of meteoroid trajectory, with ballistic coefficient-matched deceleration curve for falling sphere model shown in Fig. 8.

of 9 ± 1 Ma, as expected for a low-inclination source region that keeps the meteoroid crossing the Main Belt before impacting Earth.

However, this cannot be the full story. Both Innisfree and Villalbeto de la Peña have CRE ages much higher than their nominal collisional lifetimes (Table 14b). Also, the L5 fragmental breccia Mifflin, observed by video cameras in 2010 but without an orbit calculated, has a CRE age of 25 ± 3 Ma and original size of 60–130 cm (Kita et al. 2013), which would correspond to a collisional lifetime of 8–11 Ma. This suggests that these collisional lifetimes are underestimated for small meteoroids by about a factor of 3–5.

If so, the CRE ages of Novato and Jesenice are shorter than the collisional lifetimes. If the most recent collision changed the meteoroid size significantly, it would have resulted in a rapid evolution of the meteoroid toward a resonance, followed by an increase of eccentricity and lowering of perihelion distance, until it evolved into an Earth-crossing orbit. If so, the orbit on which the meteoroid impacts Earth will still point to the source resonance, which will restrict the range of possible source regions.

Given the orbital elements a, e, and i of Novato (Table 6b–column B, with 1σ uncertainty), the Bottke et al. (2002) model predicts a 45% probability that the meteoroid originated in the inner belt (ν6 resonance or Intermediate Mars Crossers), whereas the remaining 10% is shared between the 3:1 and the outer Main Belt. However, the Bottke et al. model applies to larger objects (>100 m), with source probabilities taken to be independent of size. Newer models, with source-dependent size distributions, show an increasing likelihood that meteoroids originate in the middle Main Belt when the size decreases.

A new model (Granvik et al. 2013) produced the dynamical timescales listed in Table 14b. The table lists the average transfer time (and standard deviation for a sample of such pathways) to go from the source resonance, to the orbit of one of the L chondrites. When a meteoroid evolves to an orbit that fulfills the criterion that $|\Delta a|$, $|\Delta e|$, and $|\Delta i|$ are less than the observed 1σ error in the orbital elements, then the orbit is considered a match and the transfer time is recorded. This transfer time from the boundary between the Near-Earth Object and Main Belt Object

Table 14b. The calculated dynamical lifetime for meteoroids originating in different source regions and being ejected from the Main Belt through different resonances. The table is divided into sources from the inner, central, and outer Main Belt. The dynamical lifetimes in bold (1σ) and italic bold (2σ) are in agreement with the measured cosmic-ray exposure (CRE) age. The measured CRE age and the calculated collisional lifetime are listed at the bottom of the table.

Resonance (Source)	Jesenice L6	Innisfree L5	Novato L6	Villalbeto de la Peña L6	Park Forest L5
Origin from inner belt					
Hungaria ($i \sim 23°$)	52.4 ± 1.8	58.1 ± 2.2	19.8 ± 3.2	31.6 ± 3.9	29.9 ± 2.4
ν6 inner ($a < 2.5$; $i < 4°$)	12.2 ± 1.0	***20.2 ± 2.3***	**9.4 ± 1.0**	11.9 ± 2.5	13.7 ± 1.3
ν6 inner ($a < 2.5$; $i > 4°$)	11.3 ± 0.8	11.2 ± 1.0	6.1 ± 0.4	13.8 ± 1.6	12.2 ± 0.7
4:1	***5.1 ± 0.6***	12.9 ± 2.2	0.9 ± 0.7	2.5 ± 0.3	3.8 ± 0.4
7:2 ($a < 2.5$ AU)	21.5 ± 2.3	18.9 ± 2.1	***28.1 ± 8.9***	15.3 ± 1.2	16.3 ± 0.6
3:1 ($a < 2.5$ AU)	7.0 ± 1.1	11.1 ± 2.6	3.5 ± 1.8	1.2 ± 0.1	0.9 ± 0.2
Origin from central belt					
ν6 inner ($a > 2.5$ AU)	**27.8 ± 22.8**	–	**15.8 ± 14.8**	~1.8	4.5 ± 2.0
7:2 ($a > 2.5$ AU)	19.5 ± 5.8	5.0 ± 2.4	**9.4 ± 5.1**	7.1 ± 3.9	14.9 ± 4.6
ν6 outer ($i \leq 18°$)	**7.1 ± 3.0**	8.7 ± 1.1	–	4.4 ± 1.4	6.8 ± 1.2
3:1 ($a > 2.5$, $i > 6°$, incl. Gefion family)	***48.1 ± 39.2***	**21.1 ± 16.8**	2.0 ± 0.6	6.8 ± 3.5	1.8 ± 0.4
3:1 (a > 2.5 AU, $i < 6°$)	***11.1 ± 5.9***	***13.9 ± 7.3***	2.7 ± 0.9	0.8 ± 0.2	0.7 ± 0.1
ν6 outer ($i > 18°$)	~24.4	13.7 ± 4.2	–	–	4.2 ± 1.5
Phocaea ($i \sim 22°$)	83.2 ± 14.6	78.6 ± 12.7	36.9 ± 15.8	**82.8 ± 38.2**	37.2 ± 8.2
Teutonia	7.5 ± 1.3	12.0 ± 2.4	3.7 ± 0.4	1.3 ± 0.1	0.7 ± 0.1
8:3	***17.7 ± 7.3***	***12.5 ± 6.4***	0.9 ± 0.5	1.0 ± 0.3	2.4 ± 0.7
5:2 (incl. Gefion)	**7.3 ± 3.4**	***9.3 ± 7.7***	**6.3 ± 3.7**	0.5 ± 0.1	0.4 ± 0.1
Origin from outer belt					
2:1	~10.7	~10.6	–	–	0.7 ± 0.5
CRE age (Ma)	3.8 ± 0.3	28 ± 3	9 ± 1[a]	48 ± 5	Unknown
Collisional life time (Ma)[b]	6.3	4.3	5.9	8.9	11.3

[a]With one collision in last 3–5 Ma.
[b]In Main Belt, based only on size: possibly underestimated by factor of 3–5 (see text).

region to the impact orbit does not include nongravitational forces.

The Main Belt phase transfer times from source to resonance were calculated by Granvik et al. (2013) based on a Yarkovsky semimajor axis drift typical for much larger (100 m sized) objects and, therefore, are not reported here. Assuming that this time is relatively short (<1 Ma), the dynamical lifetime should be similar to the measured cosmic-ray exposure age. Bold entries in Table 14b identify the various source regions and resonances that are consistent with this. We find that Novato, Jesenice, and Innisfree point to these meteoroids originating in the central belt, arriving to us from the 3:1 or the 5:2 mean-motion resonance. This scenario is consistent with these meteoroids originating from the Gefion family, but suggests that even today some shocked L chondrites may come to us directly from the 5:2 mean-motion resonance.

In this scenario, Villalbeto de la Peña should have arrived from the 3:1 or 5:2 mean-motion resonances only 6.8 ± 3.5 or 0.5 ± 0.1 Ma ago, but has a very high 48 ± 5 Ma CRE age instead (Table 14b). However, Villalbeto de la Peña was recently reclassified as a hydrothermally metamorphosed polymict L-chondritic breccia (Bischoff et al. 2013), and in light of the long CRE age may therefore have a different source region.

Of course, because of the wide range in dynamical lifetimes calculated for meteoroids of a given source region, these arguments would gain strength when many more L chondrite orbits could be measured.

Pre-Atmospheric Detection

The orbit of Novato as shown in column B of Table 6b was also used to investigate the possibility that the small Novato meteoroid may perhaps have been detected in routine asteroid surveys prior to entry into Earth's atmosphere during the last h before approach. 5,940,405 images were considered from the land-based CFHT, Spacewatch, Catalina, Mount Lemmon, Siding Springs, Pan-STARRS, and LONEOS surveys, as well as the space-based WISE, NEOWISE, HST-WFPC2, and WFC3 infrared and visible images

catalogues. No candidate detections were found. Aside from the small size, this object approached from southern latitudes, where asteroid surveys are infrequent. Assuming the estimated minimum diameter of 35 cm and an albedo of 0.15, we calculate the absolute magnitude of the object at H $\leq$ +35.0. Assuming a slope parameter of 0.15, the object's apparent magnitude was well above 24, the highest limiting magnitude of current sky surveys, until just 3 h prior to contact. A contributing factor to Novato's high magnitude was its approach from an unfavorable sun angle, with a solar elongation of 67–70° and a phase angle of 109–112° in the days prior to contact. Novato's apparent magnitude decreased to +22.6 2 h prior to contact, was +21.2 1 h prior, was +19.7 30 min prior, and would have finished at magnitude +15.8 at atmospheric contact if the Earth's shadow could be ignored.

Of particular interest with the Novato orbit is its semimajor axis of $a = 2.088 \pm 0.077$ AU. This range contains, and the mean is quite close to, the 3:1 resonance with Earth, which has $a = 3^{2/3} = 2.080$ AU. This suggests the possibility that Novato could have been perturbed by recent close encounters with Earth, even during the prior orbit. To arrive at the orbit in column (B) of Table 6b, 1000 object clones were randomly selected over the entry state uncertainties of Table 6a. When integrated back in time 3 yr to the first close encounter with Earth, 11 of the 1000 clones passed within the Hill sphere of the Earth (radius of 0.01 AU), and thus were subject to perturbations. This number is small because the observational uncertainties result in clone cloud dispersal along more than half of the object's mean orbit in the 3 yr prior to contact.

If the meteoroid was near Earth in a prior orbit, the orbit leading up to that may have been quite different. The large uncertainty in the object's position along its orbit discourages comment on the visibility of Novato on prior Earth encounters. For the encounter immediately preceding contact, only one clone passed close enough to Earth to be visible in sky survey images at that time.

CONCLUSIONS

The Novato meteorite fall occurred in a populated area and in a region where the Cameras for Allsky Meteor Surveillance project was deployed. Thanks to these circumstances, the meteorites were recovered and the preceding bolide was well documented. An accurate pre-atmospheric orbit was determined. Arriving from a southern latitude, it was not detected in Near Earth Object surveys in the hours on approach to Earth, but there is a nonzero possibility that this meteoroid was seen during a previous close encounter with Earth.

During entry, fragmentation occurred in discrete bursts coincident with flares in the lightcurve. The fragment size distribution of each debris train did not change much subsequently, but many masses (including the leading fragment) broke at the very end of their visibility period. Spallation added to the mass loss of individual fragments, possibly caused by the physical properties of a shock-blackened dark lithology that did not retain its fusion crust.

Mineral and petrochemical data and the 420 ± 220 Ma U,Th-He age point to this meteorite belonging to the shocked L chondrite group known to have had a fragmentation event approximately 470 Ma ago. Both light and dark lithologies experienced significant shock. The meteorite was slightly more compressed than other L6 chondrites of shock-stage S4. Novato is a fragmental breccia with dark and light lithologies. Although the mixture of light and dark lithologies in Novato is similar to that of regolith breccias, Novato lacks solar gases and must have formed from materials that originated from somewhat deeper inside the L chondrite parent body.

The cosmogenic radionuclide concentrations in Novato are consistent with a pre-atmospheric size of 35 ± 5 cm, consistent with the 30–60 cm diameter derived from the infrasound and optical measurements. The shielding corrected $^{21}Ne/^{26}Al$ age of 9 ± 1 Ma overlaps with a well-defined peak at approximately 10 Ma in the CRE age histogram of shocked L chondrites with low ^{40}Ar contents. However, the combination of cosmogenic radionuclides and noble gases suggests that Novato may have experienced a complex exposure history with a relatively long first-stage exposure under high shielding (resulting in the low $^{22}Ne/^{21}Ne$ ratio) and a second-stage exposure under low shielding (resulting in the low radionuclide concentrations).

Thermoluminescence data show that a reheating event (to about 200–300 °C) occurred within the last approximately 0.1 Ma. The cause of the heating is unclear. A small perihelion or atmospheric heating are clearly not the explanation, which leaves a recent shock event in space as the most likely.

These heating events may have chemically altered the organic compounds in the meteorite, but did not completely oxidize and remove all such compounds. A rich array of methanol soluble compounds and insoluble PAHs were identified. Amino acid analysis points to a low level of terrestrial contamination and that some nonprotein amino acids may be of extraterrestrial origin. The dark lithology has a higher abundance of carbon than the light lithology, with a

combustion temperature and C/N ratio that is consistent with identification of the component as amorphous to poorly crystalline carbon, possibly even microcrystalline diamond.

Together with L chondrites Jesenice and Innisfree, the orbital data are consistent with dynamical lifetimes calculated for an origin in the central Main Belt, and driven toward Earth from either the 3:1 or 5:2 mean-motion resonances. This is consistent with the proposed origin of shocked L6 chondrites in the Gefion family, but it implies that even today some L chondrites could come directly out of the 5:2 resonance.

Acknowledgments—This consortium study was made possible thanks to the donation of meteorite N01 by Novato residents Lisa Webber and Glenn Rivera. Lynn Hofland of NASA Ames Research Center performed the tensile strength measurements. This work was supported by the NASA Near Earth Object Observation and Planetary Astronomy programs (NNX12AM14G and NNX08AO64G to P.J.), the NASA Cosmochemistry program (NNG06GF95G to A.R., NNX11AJ51G to Q.Z.Y. & A.N.K., and NNX11AC69G to K.N.), and the Swiss National Science Foundation (STFC).

Editorial Handling—Dr. A. J. Timothy Jull

REFERENCES

Arpesella C. 1996. A low background counting facility at Laboratori Nazionali del Gran Sasso. *Applied Radiation and Isotopes* 47:991–996.

Baldwin B. and Sheaffer Y. 1971. Ablation and breakup of large meteoroids during atmospheric entry. *Journal of Geophysical Research* 76:4653–4668.

Beech M. 2001. Meteoroid rotation and fireball flickering: A case study of the Innisfree fireball. *Monthly Notices of the Royal Astronomical Society* 326:937–942.

Bennett M. E. and McSween H. Y. 1996. Shock features in iron-nickel metal and troilite of L-group ordinary chondrites. *Meteoritics & Planetary Science* 31: 255–264.

Benoit P. H. and Sears D. W. G. 1994. A recent meteorite fall in Antarctic with an unusual orbital history. *Earth and Planetary Science Letters* 120:463–471.

Bhandari N., Mathew K. J., Rao M. N., Herpers U., Bremer K., Vogt S., Wölfli W., Hofmann H. J., Michel R., Bodemann R., and Lange H.-J. 1993. Depth and size dependence of cosmogenic nuclide production rates in stony meteoroids. *Geochimica et Cosmochimica Acta* 57:2361–2375.

Bhandari N., Murty S. V. S., Shukla P. N., Shukla A. D., Mahajan R. R., Sarin M. M., Srinivasan G., Suthar K. M., Sisodia M. S., Jha S., and Bischoff A. 2002. Itawa Bhopji (L3–5) chondrite regolith breccia: Fall, classification, and cosmogenic records. *Meteoritics & Planetary Science* 37:549–563.

Bischoff A. and Schultz L. 2004. Abundance and meaning of regolith breccias among meteorites (abstract #5118). 67th Annual Meeting of the Meteoritical Society.

Bischoff A., Jersek M., Grau T., Mirtic B., Ott U., Kučera J., Horstmann M., Laubenstein M., Herrmann S., Randa Z., Weber M., and Heusser G. 2011. Jesenice—A new meteorite fall from Slovenia. *Meteoritics & Planetary Science* 46:793–804.

Bischoff A., Dyl K. A., Horstmann M., Ziegler K., Wimmer K., and Young E. D. 2013. Reclassification of Villalbeto de la Peña—Occurrence of a winonaite-related fragment in a hydrothermally metamorphosed polymict L-chondritic breccia. *Meteoritics & Planetary Science* 48:628–640.

Bottke W. F., Nolan M. C., and Greenberg R. 1993. Collision lifetimes and impact statistics of near-Earth asteroids. Proceedings, 24th Lunar and Planetary Science Conference. pp. 159–160.

Bottke W. F., Morbidelli A., Jedicke R., Petit J.-M., Levison H. F., Michel P., and Metcalfe T. S. 2002. Debiased orbital and absolute magnitude distribution of the near-Earth objects. *Icarus* 156:399–433.

Brearley A. J. and Jones R. H. 1998. Chondritic meteorites. In *Planetary materials*, edited by Papike J. J. Washington, D.C.: Mineralogical Society of America. pp. 3-01–3-398.

Britt D. T. and Consolmagno G. J. 2003. Stony meteorite porosities and densities: A review of the data through 2001. *Meteoritics & Planetary Science* 38:1161–1180.

Brown P., Pack D., Edwards W. N., ReVelle D. O., Yoo B. B., Spalding R. E., and Tagliaferri E. 2004. The orbit, atmospheric dynamics, and initial mass of the Park Forest meteorite. *Meteoritics & Planetary Science* 39:1781–1796.

Bunch T. E., Keil K., and Snetsinger K. G. 1967. Chromite composition in relation to chemistry and texture of ordinary chondrites. *Geochimica et Cosmochimica Acta* 31:1569–1582.

Burton A. S., Glavin D. P., Callahan M. P., Dworkin J. P., Jenniskens P., and Shaddad M. H. 2011. Heterogeneous distributions of amino acids provide evidence of multiple sources with the Almahata Sitta parent body, asteroid 2008 TC_3. *Meteoritics & Planetary Science* 46:1703–1712.

Busemann H., Bauer H., and Wieler R. 2000. Primordial noble gases in "phase Q" in carbonaceous and ordinary chondrites studied by closed-system stepped etching. *Meteoritics & Planetary Science* 35:949–973.

Ceplecha Z., Borovička J., Elford W. G., ReVelle D. O., Hawkes R. L., Porubčan V., and Simek M. 1998. Meteor phenomena and bodies. *Space Science Reviews* 84:327–471.

Christie D. R. and Campus P. 2010. The IMS infrasound network: Design and establishment of infrasound stations. In *Infrasound monitoring for atmospheric studies*, edited by Le Pichon A., Blanc E., and Hauchecorne A. Dordrecht: Springer. pp. 29–75.

Clark D. and Wiegert P. 2011. A numerical comparison with the Ceplecha analytical meteoroid orbit determination method. *Meteoritics & Planetary Science* 46:1217–1225.

Clayton R. N. and Mayeda T. K. 1984. Oxygen isotopic compositions of enstatite chondrites and aubrites. *Journal of Geophysical Research* 89:C245–C249.

Clayton R. N. and Mayeda T. K. 1996. Oxygen isotope studies of achondrites. *Geochimica et Cosmochimica Acta* 60:1999–2017.

Clayton R. N. and Mayeda T. K. 1999. Oxygen isotope studies of carbonaceous chondrites. *Geochimica et Cosmochimica Acta* 63:2089–2104.

Clayton R. N., Mayeda T. K., Goswami J. N., and Olsen E. J. 1991. Oxygen isotope studies of ordinary chondrites. *Geochimica et Cosmochimica Acta* 55:2317–2337.

Consolmagno G. J., Britt D. T., and Macke R. J. 2008. The significance of meteorite density and porosity. *Chemie der Erde* 68:1–29.

Dai J., Sun M.-Y., Culp R. A., and Noakes J. E. 2005. Changes in chemical and isotopic signatures of plant materials during degradation: Implication for assessing various organic inputs in estuarine systems. *Geophysical Research Letters* 32:L13608.

Eberhardt P., Eugster O., Geiss J., and Marti K. 1966. Rare gas measurements in 30 stone meteorites. *Zeitschrift Naturforschung Teil A* 21:414–426.

Ens T. A., Brown P. G., Edwards W. N., and Silber E. A. 2012. Infrasound production of bolides: A global statistical study. *Journal of Atmospheric Solar Terrestrial Physics* 80:208–209.

Eugster O. 1988. Cosmic-ray production rates for He-3, Ne-21, Ar-38, Kr-83, and Xe-126 in chondrites based on Kr-81/Kr exposure ages. *Geochimica et Cosmochimica Acta* 52:1649–1662.

Evans J. C., Reeves J. H., Rancitelli L. A., and Bogard D. D. 1982. Cosmogenic nuclides in recently fallen meteorites—Evidence for galactic cosmic ray variations during the period 1967–1978. *Journal of Geophysical Research* 87:5577–5587.

Everhart E. 1985. An efficient integrator that uses Gauss-Radau spacings. In *Dynamics of comets: Their origin and evolution*, edited by Carus A. and Valsecchi G. B. Proceedings of IAU Colloq. 83, Rome, Italy, June 11–15, 1984, 115: 185–202.

Evers L. G. and Haak H. W. 2001. Listening to sounds from an exploding meteor and oceanic waves. *Geophysical Research Letters* 28:41–44.

Farinella P., Vokrouhlicky D., and Harmann W. K. 1998. Meteorite delivery via Yarkovsky orbital drift. *Icarus* 132:378–387.

Friedrich J. M. and Rivers M. L. 2013. Three-dimensional imaging of ordinary chondrite microporosity at 2.6 mm resolution. *Geochimica et Cosmochimica Acta* 116:63–70.

Friedrich J. M., Wang M., and Lipschutz M. E. 2003. Chemical studies of L chondrites. V: Compositional patterns for 49 trace elements in 14 L4-6 and 7 LL4-6 falls. *Geochimica et Cosmochimica Acta* 67:2467–2479.

Friedrich J. M., Bridges J. C., Wang M.-S., and Lipschutz M. E. 2004. Chemical studies of L chondrites. VI: Variations with petrographic type and shock-loading among equilibrated falls. *Geochimica et Cosmochimica Acta* 68:2889–2904.

Friedrich J. M., Wignarajah D. P., Chaudhary S., Rivers M. L., Nehru C. E., and Ebel D. S. 2008. Three dimensional petrography of metal phases in equilibrated L chondrites—Effects of shock loading and dynamic compaction. *Earth and Planetary Science Letters* 275:172–180.

Friedrich J. M., Ruzicka A., Rivers M. L., Ebel D. S., Thostenson J. O., and Rudolph R. A. 2013. Metal veins in the Kernouvé (H6 S1) chondrite: Evidence for pre- or syn-metamorphic shear deformation. *Geochimica et Cosmochimica Acta* 116:71–83, doi:10.1016/j.gca.2013.01.009.

Glavin D. P., Dworkin J. P., Aubrey A., Botta O., Doty J. H. III, Martins Z., and Bada J. L. 2006. Amino acid analyses of Antarctic CM2 meteorites using liquid chromatography-time of flight-mass spectrometry. *Meteoritics & Planetary Science* 41:889–902.

Glavin D. P., Callahan M. P., Dworkin J. P., and Elsila J. E. 2010. The effects of parent body processes on amino acids in carbonaceous chondrites. *Meteoritics & Planetary Science* 45:1948–1972.

Göpel C. and Birck J.-L. 2010. Mn/Cr systematics: A tool to discriminate the origin of primitive meteorites? Goldschmidt Conference Abstracts. *Geochimica et Cosmochimica Acta* 74(Suppl.):A348.

Grady M. M., Wright I. P., and Pillinger C. T. 1989. A preliminary investigation into the nature of carbonaceous material in ordinary chondrites. *Meteoritics* 24:147–154.

Graf T., Baur H., and Signer P. 1990. A model for the production of cosmogenic nuclides in chondrites. *Geochimica et Cosmochimica Acta* 54:2521–2534.

Granvik M., Morbidelli A., Jedicke R., Bottke W. F., Bolin B., Beshore E., Vokrouhlicky D., Nesvorny D., and Michel P. 2013. A new population model of the orbits and absolute magnitudes of Near-Earth Objects. 45th Annual Meeting of the Division for Planetary Sciences of the American Astronomical Society, Denver, Colorado, 6–11 October 2013, AAS, meeting abstract #106.02.

Haas J. R. and Haskin L. A. 1991. Compositional variations among whole-rock fragments of the L6 chondrites Bruderheim. *Meteoritics* 26:13–26.

Halliday I., Blackwell A. T., and Griffin A. A. 1978. The Innisfree meteorite and the Canadian Camera Network. *Journal of Royal Astronomical Society of Canada* 72: 15–39.

Halliday I., Griffin A. A., and Blackwell A. T. 1981. The Innisfree meteorite fall: A photographic analysis of fragmentation, dynamics and luminosity. *Meteoritics & Planetary Science* 16:153–170.

Hartmetz C. P., Ostertag R., and Sears D. W. G. 1986. A thermoluminescence study of experimentally shock-loaded oligoclase and bytownite. Proceedings, 17th Lunar and Planetary Science Conference, Part 1. *Journal of Geophysical Research* 91:E263–E274.

Hashizume K. and Sugiura N. 1995. Nitrogen isotopes in bulk ordinary chondrites. *Geochimica et Cosmochimica Acta* 59:4057–4069.

Hertkorn N., Ruecker C., Meringer M., Gugisch R., Frommberger M., Perdue E. M., Witt M., and Schmitt-Kopplin Ph. 2007. High-precision frequency measurements: Indispensable tools at the core of the molecular-level analysis of complex systems. *Analytical Bioanalytical Chemistry* 389:1311–1327.

Heusser G., Hampel W., Kirsten T., and Schaeffer O. A. 1978. Cosmogenic isotopes in recently fallen meteorites. *Meteoritics* 13:492–493.

Irving A. J., Tanaka R., Steele A., Kuehner S. M., Bunch T. E., Wittke J. H., and Hupé G. M. 2011. Northwest Africa 6704: A unique cumulate permafic achondrite containing sodic feldspar, awaruite and "fluid" inclusions, with an oxygen isotopic composition in the Acapulcoite-Lodranite field (abstract #5231). *Meteoritics & Planetary Science* 46:A108

Jarosewich E. 1990. Chemical analyses of metorites: A compilation of stony and iron meteorite analyses. *Meteoritics* 25:323–337.

Jenniskens P. 2010. Observations of the Stardust sample return capsule entry with a slitt-less Echelle spectrograph. *Journal of Spacecraft & Rockets* 47:718–735.

Jenniskens P., Gural P. S., Dynneson L., Grigsby B. J., Newman K. E., Borden M., Koop M., and Holman D. 2011. CAMS: Cameras for Allsky Meteor Surveillance to establish minor meteor showers. *Icarus* 216:40–61.

Jenniskens P., Fries M. D., Yin Q.-Z., Zolensky M., Krot A. N., Sandford S., Sears D., Beauford R., Ebel D. S., Friedrich J. M., Nagashima K., Wimpenny J., Yamakawa A., Nishiizumi K., Hamajima Y., Caffee M. W., Welten K. C., Laubenstein M., Davis A. M., Simon S. B., Heck P. R., Young E. D., Kohl I. E., Thiemens M., Nunn M. H., Mikouchi T., Hagiya K., Ohsumi K., Cahill T. A., Lawton J. A., Barnes D., Steele A., Rochette P., Verosub K., Gattacceca J., Cooper G., Glavin D. P., Burton A. S., Dworkin J. P., Elsila J. E., Pizzarello S., Ogliore R., Schmitt-Kopplin P., Harir P., Hertkorn N., Verchovsky A., Grady M., Nagao K., Okazaki R., Takechi H., Hiroi T., Smith K., Silber E. A., Brown P. G., Albers J., Klotz D., Hankey M., Matson R., Fries J. A., Walker R. J., Puchtel I., Lee C.-T. A., Erdman M., Eppich G. R., Roeske S., Gabelica Z., Lerche M., Nuevo M., Girten B., and Worden S. P. (the Sutter's Mill Meteorite Consortium) 2012. Radar-enabled recovery of the Sutter's Mill meteorite, a carbonaceous chondrite regolith breccia. *Science* 338:1583–1587.

Kita N. T., Welten K. C., Valley J. W., Spicuzza M. J., Nakashima D., Tenner T. J., Ushikubo T., MacPherson G. J., Welzenbach L., Heck P. R., Davis A. M., Meier M. M. M., Wieler R., Caffee M. W., Laubenstein M., and Nishiizumi K. 2013. Fall classification, and exposure history of the Mifflin L5 chondrite. *Meteoritics & Planetary Science* 48:641–655.

Kleber M., Sollins P., and Sutton R. 2007. A conceptual model of organo-mineral interactions in soils: Self assembly of organic molecular fragments into zonal structures on mineral surfaces. *Biogeochemistry* 85:9–24.

Kohman T. P. and Bender M. L. 1967. Nuclide production by cosmic rays in meteorites and on the Moon. High-energy nuclear reactions in astrophysics. In *High-energy nuclear reactions in astrophysics—A collection of articles*, edited by Shen B. S. P. New York: W. A. Benjamin. pp. 169–245.

Korochantseva E. V., Trieloff M., Lorenz C. A., Buykin A. I., Ivanova M. A., Schwarz W. H., Hopp J., and Jessberger E. K. 2007. L-chondrite asteroid breakup tied to Ordovician meteorite shower by multiple isochron ^{40}Ar-^{39}Ar dating. *Meteoritics & Planetary Science* 42:113–130.

Le Guillou C., Rouzaud J.-N., Bonal L., Quirico E., Derenne S., and Remusat L. 2012. High resolution TEM of chondritic carbonaceous matter: Metamorphic evolution and heterogeneity. *Meteoritics & Planetary Science* 47:345–362.

Leya I. and Masarik J. 2009. Cosmogenic nuclides in stony meteorites revisited. *Meteoritics & Planetary Science* 44:1061–1086.

Llorca J., Trigo-Rodríguez J. M., Ortiz J. L., Docobo J. A., García-Guinea J., Catro-Tirado A. J., Rubin A. E., Eugster O., Edwards W., Laubenstein M., and Casanova I. 2005. The Villalbeto de la Peña meteorite fall: I. Fireball energy, meteorite recovery, strewn field, and petrography. *Meteoritics & Planetary Science* 40:795–804.

Lodders K. 2003. Solar system abundances and condensation temperatures of the elements. *The Astrophysical Journal* 591:1220–1247.

Lodders K., Palme H., and Gail H. P. 2009. Abundances of the elements in the solar system. In *solar system*, edited by Truemper J. E. Berlin: Springer. pp. 560–630.

Marchand C., Disnar J. R., Lallier-Vergès E., and Lottier N. 2005. Early diagenesis of carbohydrates and lignin in mangrove sediments subject to variable redox conditions (French Guiana). *Geochimica et Cosmochimica Acta* 69:131–142.

Marti K. and Graf T. 1992. Cosmic-ray exposure history of ordinary chondrites. *Annual Review of Earth and Planetary Sciences* 20:221–243.

Mason B. and Graham A. L. 1970. Minor and trace elements in meteoritic minerals. *Smithsonian Contribution to the Earth Sciences* 3:1–17.

Meier M. M. M., Welten K. C., Caffee M. W., Friedrich J. M., Jenniskens P., Nishiizumi K., Shaddad M., and Wieler R. 2012. A noble gas and cosmogenic radionuclide analysis of two ordinary chondrites from Almahata Sitta. *Meteoritics & Planetary Science* 47:1075–1086.

Morbidelli A. and Gladman B. 1998. Orbital and temporal distributions of meteorites originating in the asteroid belt. *Meteoritics & Planetary Science* 33:999–1016.

Morden S. J. and Collinson D. W. 1992. The implications of the magnetism of ordinary chondrite meteorites. *Earth and Planetary Science Letters* 109:185–204.

Nesvorný D., Vokrouhlický D., Morbidelli A., and Bottke W. F. 2009. Asteroidal source of L chondrite meteorites. *Icarus* 200:698–701.

Nishiizumi K. 2004. Preparation of ^{26}Al AMS standards. *Nuclear Instruments and Methods in Physics Research* B223–224:388–392.

Nishiizumi K., Regnier S., and Marti K. 1980. Cosmic ray exposure ages of chondrites, pre-irradiation and constancy of cosmic ray flux in the past. *Earth and Planetary Science Letters* 50:156–170.

Nishiizumi K., Imamura M., Caffee M. W., Southon J. R., Finkel R. C., and McAninch J. 2007. Absolute calibration of ^{10}Be AMS standards. *Nuclear Instruments and Methods in Physics Research* B258:403–413.

Ott U., Herrmann S., Haack H., and Gau T. 2010. Noble gases in two meteorites that fell in Denmark and Slovenia in 2009 (abstract #1196). 41st Lunar and Planetary Science Conference. CD-ROM.

Popova O. P., Jenniskens P., Emel'yanenko V., Kartashova A., Biryukov E., Khaibrakhmanov S., Shuvalov V., Rybnov Y., Dudorov A., Grokhovsky V. I., Badyukov D. D., Yin Q.-Z., Gural P. S., Albers J., Granvik M., Evers L. G., Kuiper J., Kharlamov V., Solovyov A., Rusakov Y. S., Korotkiy S., Serdyuk I., Korochantsev A. V., Larionov M. Y., Glazachev D., Mayer A. E., Gisler G., Gladkovsky S. V., Wimpenny J., Sanborn M. E., Yamakawa A., Verosub K., Rowland D. J., Roeske S., Botto N. W., Friedrich J. M., Zolensky M., Le L., Ross D., Ziegler K., Nakamura T., Ahn I., Lee J. I., Zhou Q., Li X.-H., Li Q.-L., Liu Y., Tang G.-Q., Hiroi T., Sears D., Weinstein I. A., Vokhmintsev A. S., Ishchenko A. V., Schmitt-Kopplin P., Hertkorn N., Nagao K., Haba M. K., Komatsu M., and Mikouchi T. (the Chelyabinsk Airburst Consortium). 2013. Chelyabinsk airburst, damage assessment, meteorite recovery, and characterization. *Science* 342:1069–1073.

Qin L., Alexander C. M. O'D., Carlson R. W., Horan M. F., and Yokoyama T. 2010. Contributors to chromium isotope variation of meteorites. *Geochimica et Cosmochimica Acta* 74:1122–1145.

Quirico E., Raynal P. I., and Bourot-Denise M. 2003. Metamorphic grade of organic matter in six unequilibrated

ordinary chondrites. *Meteoritics & Planetary Science* 38:795–811.
Remusat L., Derenne S., and Robert F. 2005. New insights on aliphatic linkages in the macromolecular organic fraction of Orgueil and Murchison meteorites through ruthenium tetroxide oxidation. *Geochimica et Cosmochimica Acta* 69:4377–4386.
ReVelle D. O. 2002. Fireball dynamics, energetics, ablation, luminosity, and fragmentation modeling. In *Proceedings of the Conference Asteroids, Comets, Meteors (ACM 2002)*, edited by Warmbein B. ESA SP-500. Noordwijk: European Space Research and Technology Research Center. pp. 127–136.
ReVelle D. O. 2007. NEO fireball diversity: Energetics-based entry modeling and analysis techniques. *Proceedings of the International Astronomical Union Symposium* 236:95–106.
ReVelle D. O. and Ceplecha Z. 2001. Bolide physical theory with application to PN and EN fireballs. *ESA Special Publication* 495:507–512.
Rochette P., Sagnotti L., Bourout-Denise M., Consolmagno G., Folco L., Gattacceca J., Osete M. L., and Pesonen L. 2003. Magnetic classification of stony meteorites: 1. Ordinary chondrites. *Meteoritics & Planetary Science* 38:251–268.
Rubin A. E. 1990. Kamacite and olivine in ordinary chondrites: Intergroup and intragroup relationships. *Geochimica et Cosmochimica Acta* 54:1217–1232.
Rubin A. E. 1992. A shock-metamorphic model for silicate darkening and compositionally variable plagioclase in CK and ordinary chondrites. *Geochimica et Cosmochimica Acta* 56:1705–1714.
Rubin A. E. 2003. Chromite-plagioclase assemblages as a new shock indicator: Implications for the shock and thermal histories of ordinary chondrites. *Geochimica et Cosmochimica Acta* 67:2695–2709.
Rubin A. E., Peterson E., Keil K., Rehfeldt A., and Jarosewich E. 1983. Fragmental breccias and the collisional evolution of ordinary chondrite parent bodies. *Meteoritics* 18:179–196.
Russell S. S., Arden J., and Pillinger C. T. 1991. Evidence for multiple sources of diamond from primitive chondrites. *Science* 254:1188–1191.
Schmitt R. T., Deutsch A., and Stöffler D. 1993. Shock effects in experimentally shocked samples of the H6 chondrite Kernouvé (abstract). *Meteoritics* 28:431–432.
Schmitt-Kopplin P., Gabelica Z., Gougeon R. D., Fekete A., Kanawati B., Harir M., Gebefuegi I., Eckel G., and Hertkorn N. 2010. High molecular diversity of extraterrestrial organic matter in Murchison meteorite revealed 40 years after its fall. *Proceedings of the National Academy of Sciences* 107:2763–2768.
Schmitt-Kopplin P., Harir M., Kanawati B., Tziotis D., Hertkron N., and Gabelica Z. 2012. Chemical footprint of the solvent soluble extraterrestrial organic matter occluded in Soltmany ordinary chondrite. *Meteorites* 2:79–92.
Schmitz B., Tassinari M., and Peucker-Ehrenbrink B. 2001. A rain of ordinary chondritic meteorites in the early Ordovician. *Earth and Planetary Science Letters* 194:1–15.
Schneider D. M., Hartmann W. K., Benoit P. H., and Sears D. W. G. 2000. Fusion crust simulation and the search for Martian sediments on earth (abstract #1388). 31st Lunar and Planetary Science Conference. CD-ROM.
Schoonen M., Smirnov A., and Cohn C. 2004. A perspective on the role of minerals in prebiotic synthesis. *Ambio* 33:539–551.
Sears D. W. G. 1978. *The nature and origin of meteorites*. New York: Oxford UP. pp. 34–38.
Sears D. W. G. and Mills A. A. 1973. Temperature gradients and atmospheric ablation rates for the Barwell meteorite. *Nature Physical Science* 242:25–26.
Sears D. W. G., Grossman J. N., Melcher C. L., Ross L. M., and Mills A. A. 1980. Measuring metamorphic history of unequilibrated ordinary chondrites. *Nature* 287:791–795.
Sears D. W. G., Ninagawa K., and Signhvi A. 2013. Luminescence studies of extraterrestrial materials: Insights into their recent radiation and thermal histories and into their metamorphic history. *Chemie der Erde* 73:1–37.
Sharma P., Bourgeous M., Elmore D., Granger D., Lipschutz M. E., Ma X., Miller T., Mueller K., Rickey F., Simms P., and Vogt S. 2000. PRIME lab AMS performance, upgrades and research applications. *Nuclear Instruments and Methods in Physics Research* B172:112–123.
Simon S. B., Grossman L., Clayton R. N., Mayeda T. K., Schwade J. R., Sipiera P. P., Wacker J. F., and Wadhwa M. 2004. The fall, recovery, and classification of the Park Forest meteorite. *Meteoritics & Planetary Science* 39:625–634.
Slyuta E. N. 2010. Physical-mechanical anisotropy of ordinary chondrites and the shape of small rocky bodies (abstract #1103). 41st Lunar and Planetary Science Conference. CD-ROM.
Spergel M. S., Reedy R. C., Lazareth O. W., Levy P. W., and Slatest L. A. 1986. Cosmogenic neutron-capture-produced nuclides in stony meteorites. *Journal of Geophysical Research* 91:483–494.
Spurný P., Borovička J., Kac J., Kalenda P., Atanackov J., Kladnik G., Heinlein D., and Grau T. 2010. Analysis of instrumental observations of the Jesenice meteorite fall on April 9, 2009. *Meteoritics & Planetary Science* 45:1392–1407.
Stöffler D., Keil K., and Scott E. R. D. 1991. Shock metamorphism of ordinary chondrites. *Geochimica et Cosmochimica Acta* 55:3845–3867.
Trigo-Rodríguez J. M., Borovička J., Spurný P., Ortiz J. L., Docobo J. A., Castro-Tirado A. J., and Llorca J. 2006. The Villalbeto de la Peña meteorite fall: II. Determination of atmospheric trajectory and orbit. *Meteoritics & Planetary Science* 41:505–517.
Trinquier A., Birck J.-L., and Allègre C. J. 2007. Widespread ^{54}Cr heterogeneity in the inner solar system. *The Astrophysical Journal* 655:1179–1185.
Trinquier A., Birck J.-L., Allègre C. J., Göpel C., and Ulfbeck D. 2008. ^{53}Mn–^{53}Cr systematics of the early solar system revisited. *Geochimica et Cosmochimica Acta* 72:5146–5163.
Troiano J., Rumble D. III, Rivers M. L., and Friedrich J. M. 2011. Compositions of three low-FeO ordinary chondrites: Indications of a common origin with the H chondrites. *Geochimica et Cosmochimica Acta* 75:6511–6519.
Van Schmus W. R. and Ribbe P. H. 1968. The composition and structural state of feldspar from chondritic meteorites. *Geochimica et Cosmochimica Acta* 32:1327–1342.
Van Schmus W. R. and Wood J. A. 1967. A chemical-petrologic classification for the chondritic meteorites. *Geochimica et Cosmochimica Acta* 31:747–765.

Wasson J. T. and Kallemeyn G. W. 1988. Compositions of chondrites. No. 1587. The solar system: Chemistry as a Key to Its Origin. *Philosophical Transactions of the Royal Society of London. Series A, Mathematical and Physical Sciences* 325:535–544.

Weirich J. R., Swindle T. D., and Isachsen C. E. 2012a. ^{40}Ar–^{39}Ar age of Northwest Africa 091: More evidence for a link between L chondrites and fossil meteorites. *Meteoritics & Planetary Science* 47:1324–1335.

Weirich J. R., Swindle T. D., Isachsen C. E., Sharp T. G., Li C., and Downs R. T. 2012b. Source of potassium in shocked ordinary chondrites. *Geochimica et Cosmochimica Acta* 98:125–139.

Wetherhill G. 1985. Asteroidal source of ordinary chondrites. *Meteoritics* 20:1–22.

Wieler R., Graf T., Pedroni A., Signer P., Pellas P., Fieni C., Suter M., Vogt S., Clayton R. N., and Laul J. C. 1989. Exposure history of the regolithic chondrite Fayetteville. II—Solar-gas-free light inclusions. *Geochimica et Cosmochimica Acta* 53:1449–1459.

Woodcock N. H. 1977. Specification of fabric shapes using an eigenvalue method. *Geological Society of America Bulletin* 88:1231–1236.

Woodcock N. H. and Naylor M. A. 1983. Randomness testing in three-dimensional orientation data. *Journal of Structural Geology* 5:539–548.

Wu Q., Pomerantz A., Mullins O., and Zare R. N. 2013. Minimization of fragmentation and aggregation by laser desorption laser ionization mass spectrometry. *Journal of the American Society for Mass Spectrometry* 24:1116–1122.

Yamakawa A., Yamashita K., Makishima A., and Nakamura E. 2010. Chromium isotope systematics of achondrites: Chronology and isotopic heterogeneity of the inner solar system bodies. *The Astrophysical Journal* 720:150–154.

Yin Q.-Z., Zhou Q., Li Q.-L., Li X.-H., Tang G.-Q., Krot A. N., and Jenniskens P. 2014. Records of the Moon-forming impact and the disruption of the L-chondrite parent body from U-Pb apatite ages of Novato (L6). *Meteoritics & Planetary Science*, doi: xxxx.

Young E. D. and Russell S. S. 1998. Oxygen reservoirs in the early solar nebula inferred from an Allende CAI. *Science* 282:452–455.

Zinner E. 1988. Interstellar cloud material in meteorites. In *Meteorites and the early solar system*, edited by Kerridge J. F. and Mathews M. S. Tucson, Arizona: The University of Arizona Press. pp. 956–983.